AGU PUBLICATIONS

Geochemistry, Geophysics, Geosystems

RESEARCH ARTICLE
10.1002/2015GC005947

Architecture of North Atlantic contourite drifts modified by transient circulation of the Icelandic mantle plume

Ross Parnell-Turner[1,2], Nicholas J. White[1], I. Nick McCave[1], Timothy J. Henstock[3], Bramley Murton[3], and Stephen M. Jones[4]

[1]Department of Earth Sciences, University of Cambridge, Cambridge, UK, [2]Now at Woods Hole Oceanographic Institution, Woods Hole, Massachusetts, USA, [3]National Oceanography Centre, University of Southampton, Waterfront Campus, European Way, Southampton, UK, [4]School of Geography, Earth and Environmental Sciences, University of Birmingham, Birmingham, UK

Key Points:
- Seismic reflection profiles of contourite drifts in North Atlantic Ocean
- Sedimentary accumulation rate of drift deposits varies with time
- Dynamic support from Iceland plume controls deep-water flow and drift evolution

Supporting Information:
- Supporting Information S1

Correspondence to:
R. Parnell-Turner and N. White,
rparnellturner@whoi.edu and
njw10@cam.ac.uk

Citation:
Parnell-Turner, R., N. J. White, I. N. McCave, T. J. Henstock, B. Murton, and S. M. Jones (2015), Architecture of North Atlantic contourite drifts modified by transient circulation of the Icelandic mantle plume, *Geochem. Geophys. Geosyst.*, *16*, 3414–3435, doi:10.1002/2015GC005947.

Received 5 JUN 2015
Accepted 18 SEP 2015
Accepted article online 23 SEP 2015
Published online 15 OCT 2015

Abstract Overflow of Northern Component Water, the precursor of North Atlantic Deep Water, appears to have varied during Neogene times. It has been suggested that this variation is moderated by transient behavior of the Icelandic mantle plume, which has influenced North Atlantic bathymetry through time. Thus pathways and intensities of bottom currents that control deposition of contourite drifts could be affected by mantle processes. Here, we present regional seismic reflection profiles that cross sedimentary accumulations (Björn, Gardar, Eirik, and Hatton Drifts). Prominent reflections were mapped and calibrated using a combination of boreholes and legacy seismic profiles. Interpreted seismic profiles were used to reconstruct solid sedimentation rates. Björn Drift began to accumulate in late Miocene times. Its average sedimentation rate decreased at ~2.5 Ma and increased again at ~0.75 Ma. In contrast, Eirik Drift started to accumulate in early Miocene times. Its average sedimentation rate increased at ~5.5 Ma and decreased at ~2.2 Ma. In both cases, there is a good correlation between sedimentation rates, inferred Northern Component Water overflow, and the variation of Icelandic plume temperature independently obtained from the geometry of diachronous V-shaped ridges. Between 5.5 and 2.5 Ma, the plume cooled, which probably caused subsidence of the Greenland-Iceland-Scotland Ridge, allowing drift accumulation to increase. When the plume became hotter at 2.5 Ma, drift accumulation rate fell. We infer that deep-water current strength is modulated by fluctuating dynamic support of the Greenland-Scotland Ridge. Our results highlight the potential link between mantle convective processes and ocean circulation.

1. Introduction

At important oceanic gateways such as the Greenland-Iceland-Scotland Ridge, pathways and intensities of oceanic bottom currents are influenced by bathymetric configuration. In turn, this configuration is modulated by changes in dynamic support beneath subsiding lithospheric plates [e.g., *Vogt*, 1972; *Poore et al*., 2006]. At the present day, warm, saline surface water of the North Atlantic Current flows into the Norwegian Sea [*Mauritzen*, 1996]. This surface water eventually cools, sinks, and returns southward as Norwegian Sea Deep Water [*Hansen and Østerhus*, 2000]. Deep water mixes with shallower water as it crosses the Iceland-Faroe Ridge and the Faroe Bank Channel. It then forms Iceland-Scotland Overflow Water (ISOW), which has a flux of 3.4 Sverdrups (1 Sv = 1×10^6 m^3s^{-1}) and represents a precursor of North Atlantic Deep Water (NADW; Figure 1a).

Cold deep water also flows through the Denmark Strait, delivering 3 Sv of Denmark Strait Overflow Water (DSOW) into the Irminger Basin [*Hansen and Østerhus*, 2000]. Production of this deep flow is an important component of the Atlantic Meridional Overturning Circulation (AMOC) [*Broecker and Denton*, 1989]. Suppression of NADW formation during glacial periods was associated with extensive sea ice cover over regions where deep waters form in the Norwegian Sea [e.g., *Kellogg*, 1980; *Boyle and Keigwin*, 1982]. Input of saline Mediterranean Outflow Water could also affect formation of these deep water masses [*Reid*, 1979; *Khélifi et al*., 2009].

In Neogene times, vertical motions at this oceanic gateway may have moderated flux of ISOW into the North Atlantic Ocean [*Wright and Miller*, 1996; *Poore et al*., 2006, 2011]. Following a suggestion by *Wright*

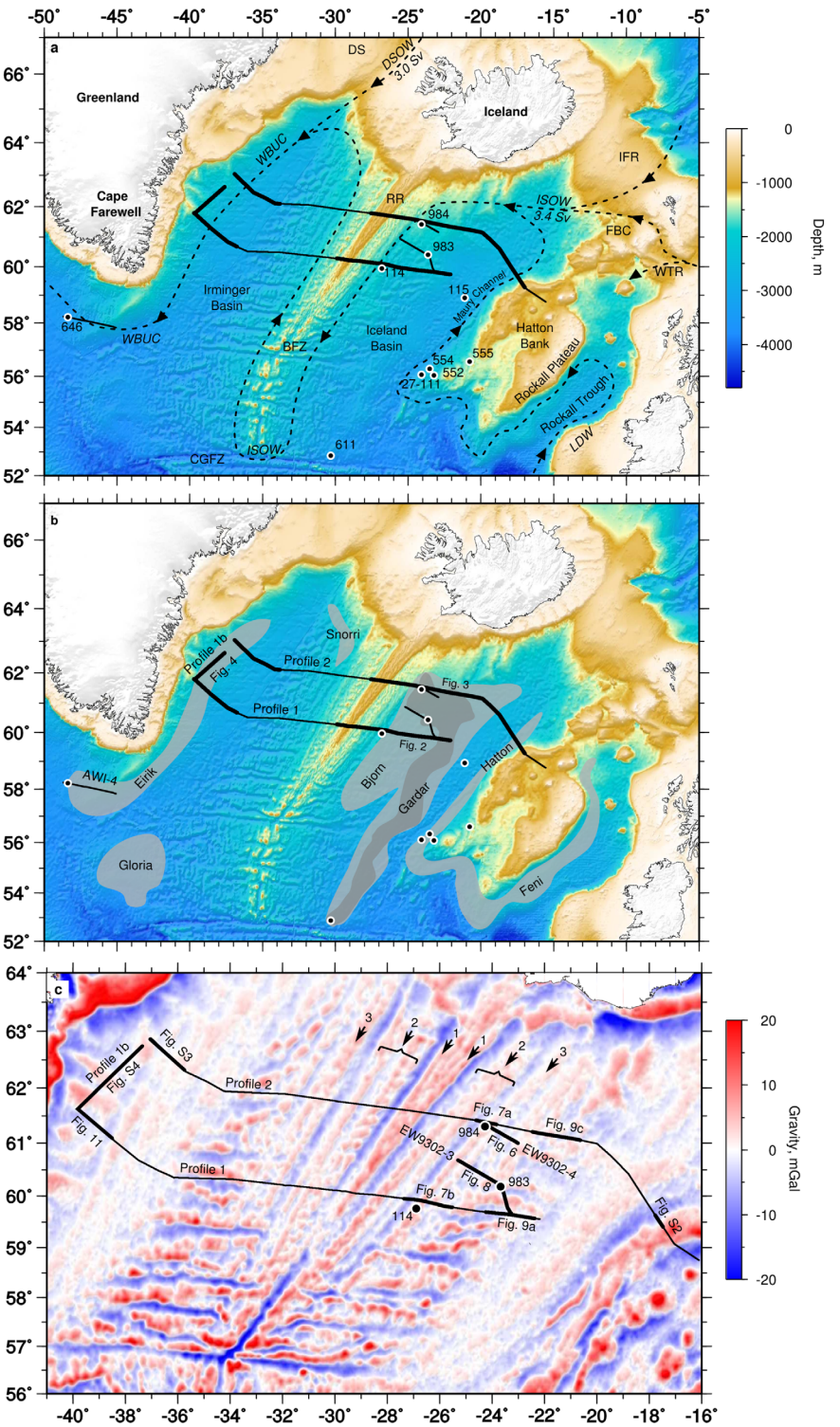

Figure 1. Bathymetry and gravity of north Atlantic Ocean showing location of JC50 seismic reflection survey. (a) Thick solid lines = JC50 seismic profiles (bold portions shown in Figures 2–4); thin solid lines = seismic data used for well-ties; numbered circles = drilling locations; labeled dashed lines = deep-water currents and their rates [*Hansen and Østerhus*, 2000; *Olsen et al.*, 2008]; DS = Denmark Strait; IFR = Iceland-Faroe Ridge; FBC = Faroe Bank Channel; WTR = Wyville Thomson Ridge; LDW = Lower Deep Water; BFZ = Bight Fracture Zone; RR = Reykjanes Ridge; and CGFZ = Charlie-Gibbs Fracture Zone. (b) Light gray shading = contourite drift deposits [*Faugères et al.*, 1999]; dark gray shading = areas of present-day drift sedimentation identified using 3.5 kHz acoustic profiles [*Bianchi and McCave*, 2000]. (c) High-pass (< 250 km) free-air gravity anomaly map [*Sandwell et al.*, 2014]. Labeled bold lines = location of later figures; numbered arrows = VSRs [*Parnell-Turner et al.*, 2014].

and Miller [1996], *Poore et al*. [2006] demonstrated that there is a negative correlation between percentage of northern Component Water (%NCW) and vertical motion of the Greenland-Iceland-Scotland Ridge during Neogene times. For example, there is an increase in %NCW overflow between 6 and 2 Ma, when regional dynamic uplift provided by the Icelandic plume was weakest [*Poore et al*., 2011]. These observations can be used to establish a connection between varying deep-water current strength and changes in dynamic support beneath the lithospheric plate. There is growing evidence that dynamic support of this region is related to transient activity of the Icelandic plume, which appears to have waxed and waned over the last 55 Ma [*Jones et al*., 2002; *Parkin and White*, 2008; *Parnell-Turner et al*., 2014]. Here, we test the hypothesis that spatial and temporal accumulation of sedimentary drifts in the North Atlantic Ocean is moderated by transient support of the Iceland mantle plume.

1.1. Sedimentary Drifts

Drift deposits are conspicuous products of currents associated with deep-water overflow (Figure 1b) [*Stow and Holbrook*, 1984; *McCave and Tucholke*, 1986]. Sediment is carried by deep-water currents into the Iceland Basin where it is deposited by ISOW as two elongate sedimentary bodies, Björn and Gardar Drifts, on the eastern flank of the Reykjanes Ridge [*Egloff and Johnson*, 1979; *Johnson and Schneider*, 1969]. Hatton Drift is deposited by Lower Deep Water and ISOW flowing northward along the western side of Rockall Plateau [*Ruddiman*, 1972; *McCave et al*., 1980; *McCartney*, 1992]. Further west, Eirik Drift is deposited by the Western Boundary Under Current (WBUC = ISOW + DSOW) along the continental slope near the southern tip of Greenland at Cape Farewell (Figure 1b) [*Hunter et al*., 2007; *Müller-Michaelis et al*., 2013; *Müller-Michaelis and Uenzelmann-Neben*, 2014]. All of these deposits are typical examples of mounded, or elongate-mounded drifts whose elongation and progradation depends upon the interaction between bathymetric slope and curvature, current intensity, and thermohaline circulation [*Laberg et al*., 2005; *Rebesco and Camerlenghi*, 2008].

Thus contourite drift bodies indirectly record changes in deep-water currents and so can be used as a proxy for changes in oceanic circulation [*Wold*, 1994; *McCave and Hall*, 2006]. Variations in current activity and in sedimentary supply govern accumulation rate of a given drift, which in turn is the dominant external control for development of its stratigraphic architecture. Internally, drifts have subparallel, weak reflections, which change gradationally between seismic facies and record lateral migration of the sedimentary body [*Faugères et al*., 1999; *Nielsen et al*., 2008; *Koenitz et al*., 2008]. Depositional units are usually lenticular with convex-upward geometries that are not parallel to the accumulation surface generated by a preceding erosional event [*Faugères et al*., 1999]. Hence mappable seismic reflections represent periods when sediment supply and/or composition has changed or when nondeposition or erosion has taken place. These events permit a given drift to be subdivided into discrete, mappable units [*Cunningham et al*., 2002].

1.2. Northern Component Water and Dynamic Support

Poore et al. [2006] assembled a global inventory of δ^{13}C measurements from benthic foraminifera that can be used to characterize isotopic gradients between NCW, Southern Ocean Water, and Pacific Ocean Water. Elevation changes at the Denmark Strait and at the Iceland-Faroe Ridge appear to modulate flux of NCW into the Southern Ocean. When dynamic support of the Icelandic plume decreases, these gateways subside and a greater volume of deep water flows into the Irminger and Iceland Basins. When dynamic support increases, the gateways shoal and deep-water export is reduced. *Poore et al*. [2006] argued that reasonable estimates of %NCW can only be made post 12 Ma when δ^{13}C patterns for the three water masses diverge. This divergence is probably associated with submergence of the Denmark Strait and Iceland-Faroe Ridge. The most robust estimate of %NCW is between 7.5 and the present day.

The inferred variation of %NCW can be tested using an independent record of convective dynamic support from the North Atlantic Ocean that is obtained by analyzing the diachronous pattern of V-shaped ridges (VSRs) which straddle the Reykjanes Ridge (Figure 1c) [*Vogt*, 1971; *Jones et al*., 2002; *Poore et al*., 2009; *Parnell-Turner et al*., 2014]. VSR morphology reflects bathymetric changes which in turn are caused by crustal thickness variations of $\pm$2 km. It is generally accepted that they are generated by thermal anomalies that flow radially away from the center of the Iceland mantle plume [*Smallwood and White*, 1998]. Along the Reykjanes Ridge itself, crustal thickness measurements and the geochemical composition of dredged basaltic samples can be accounted for by potential temperature anomalies of $T_p = \pm 25^{\circ}$C beneath the

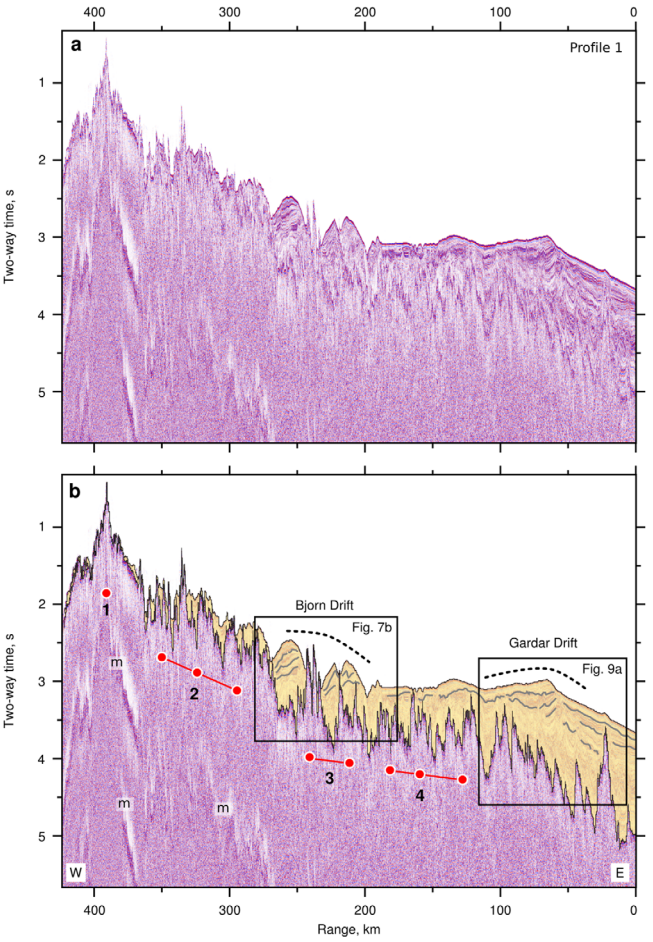

Figure 2. Portion of profile 1 (see Figure 1 for location). (a) Uninterpreted time-migrated image. (b) Interpretation. Yellow shading and gray lines = sedimentary strata; dotted lines = major drift deposits; solid line = sediment-basement interface; numbered red circles/lines = V-shaped ridges; and m = water-bottom multiple reflection. Inset boxes shown in Figures 7b and 9a. Reduced amplitudes near multiple energy caused by window size used for automatic gain control.

cooling lithospheric plate [*Murton et al.*, 2002; *Poore et al.*, 2011; *Jones et al.*, 2014]. Thermal anomalies probably occur within an asthenospheric layer which is 150 ± 50 km thick, generating bathymetric anomalies of several hundred meters [*Delorey et al.*, 2007; *Parnell-Turner et al.*, 2013]. In this way, the bathymetric configuration of oceanic gateways such as the Denmark Strait and the Iceland-Faroe Ridge can be modified [*Wright and Miller*, 1996; *Poore et al.*, 2006].

Parnell-Turner et al. [2014] established a revised chronology of plume potential temperature for the last 55 Ma. They show that temperature fluctuations occur every 3–8 Ma over distances of 1000 km. This record is an important, albeit indirect, proxy for the evolving bathymetric configuration of the Denmark Strait and Iceland-Faroe Ridge.

2. Seismic Reflection Profiles

Regional seismic reflection profiles were acquired across the Iceland and Irminger Basins on RRS *James Cook* during July–August 2010 (Figure 1). Acoustic energy was generated using a single generator-injector (GI) airgun with a volume of 5.82 l (generator and injector pulses = 4.1 and 1.72 L, respectively) and a frequency bandwidth of 10–400 Hz. The airgun was towed at a depth of 5.5 m behind the vessel, which travelled at 2 m s^{-1}. It was primed with compressed air at a pressure of 20.7 MPa and fired every 15 s (~40 m). Reflected acoustic energy was recorded along a 1.6 km long streamer towed at 7 m depth that consisted of 132 groups of hydrophones at intervals of 12.5 m. Distance from the airgun to the first group (i.e., near-trace offset) was 163 m and the sampling interval of recorded signals was 1 ms. A standard processing sequence was used. Shot point gathers were converted into common midpoint (CMP) gathers spaced every 6.25 m. Prior to stacking, root-mean-square velocities were picked every 100 CMPs (i.e., every 625 m). A 12 Hz high-pass filter with a roll-off of 24 dB per octave was applied after stacking. Images were migrated using a post stack frequency-wave number (i.e., *f-k*) algorithm with a constant velocity of 1.5 km s^{-1} [*Stolt*, 1978]. The resultant 21-fold stacked image has a vertical and horizontal resolution of 10–20 m.

Portions of the two principal flow lines, profiles 1 and 2, that traverse the Iceland Basin are shown in Figures 2 and 3 (complete profiles are shown in supporting information Figure S1). Björn and Gardar Drifts are visible on both profiles. The relationship between bathymetry, crustal structure, and depositional loci is evident. On profile 1, the western edge of Björn Drift is bounded by a prominent VSR at a range of 270 km where a channel has been carved (Figure 2b). This drift is underlain by several smaller VSRs. As a result, this composite drift has been compartmentalized into a series of subdrifts, each of which is bounded along its eastern edge by a small channel. On profile 2, a more coherent Björn Drift is perched between two VSRs at a range of 720–790 km (Figure 3b). It is separated from Gardar Drift by a 100 km wide trough.

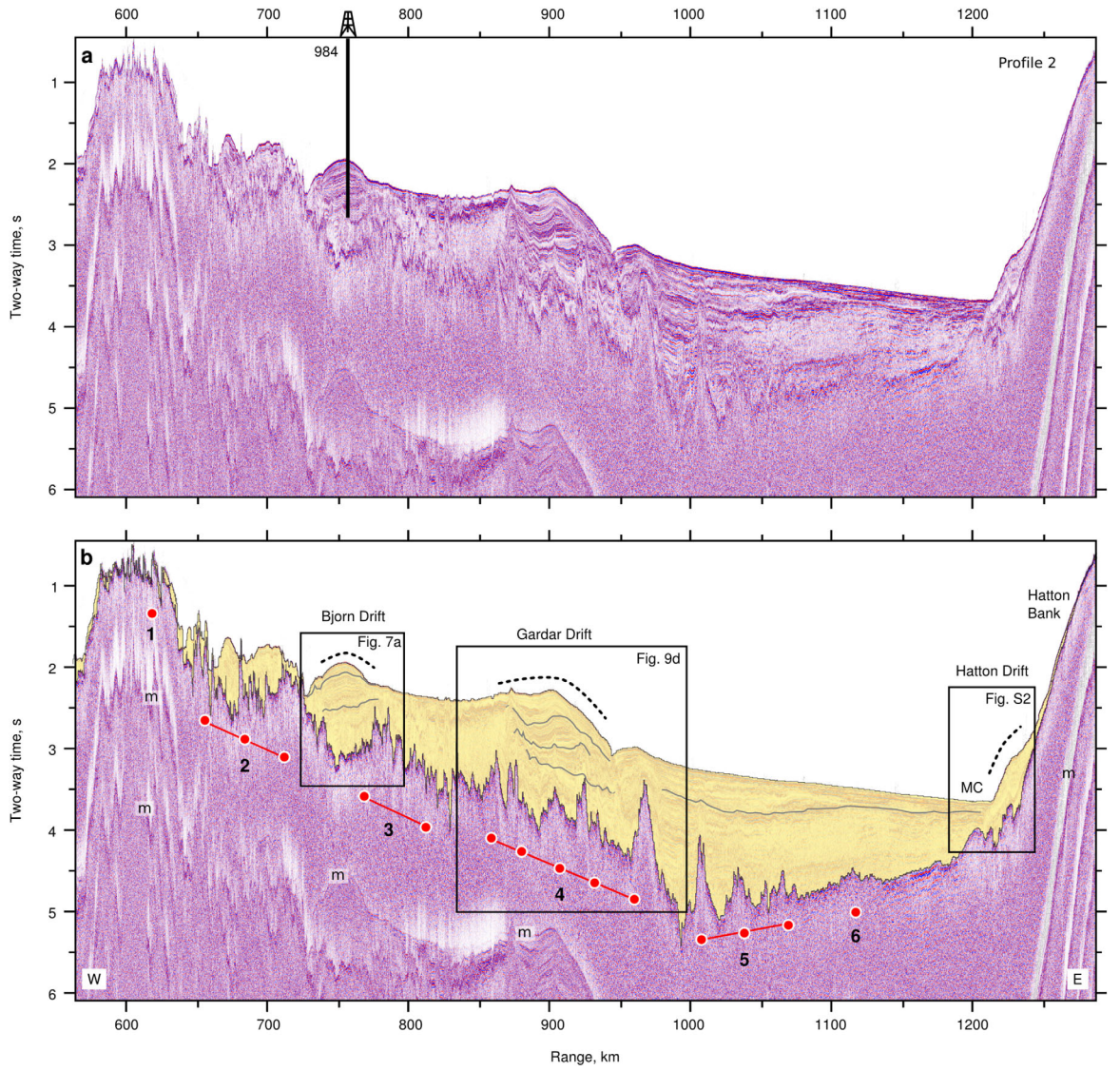

Figure 3. Portion of profile 2 (see Figure 1 for location). (a) Uninterpreted time-migrated image, showing location of ODP Leg 105 Site 984 (b) Interpretation. Yellow shading and gray lines = sedimentary strata; dotted lines = major drift deposits; black line = sediment-basement interface; numbered red circles/lines = V-shaped ridges; MC = Maury Channel; and m = water-bottom multiple reflection. Inset boxes shown in shown in Figures 7a, 9d, and S2.

The crest of the prominent Gardar Drift is identifiable at a range of 60 km on profile 1 and at a range 900 km on profile 2 (Figures 2 and 3, respectively). This drift grew on top of an irregular sediment-basement interface which has several mappable VSRs. Its deeper portion indicates that it too was originally compartmentalized between VSRs. Its shallower portion has a simpler geometry. On profile 2, a channel marks the eastern edge of this drift at a range of 945 km (Figure 3). Hatton Bank occurs at the eastern end of profile 2 where bathymetry shoals from 2500 m to 600 m over a distance of less than 100 km. Hatton Drift is positioned on the western slope of Hatton Bank and extends 30 km eastward of Maury Channel at a range of 1210–1240 km (Figure 3b and supporting information Figure S2).

Eirik Drift, which is plastered onto the East Greenland margin, is imaged by a composite profile (Figure 4). It thickens from north to south and is distributed over many hundreds of kilometers. This drift is visible on profile 1 where it lies on top of an older pile of sediments sitting on a smooth sediment-basement interface (Figure 4a). On profile 2, the eastern edge of a thinner and less extensive Eirik Drift is bounded by a prominent channel (Figure 4c and supporting information Figure S3). The connecting profile 1b reveals filled turbidity current channels cut into an older pile of sediments (Figures 4b and supporting information S4).

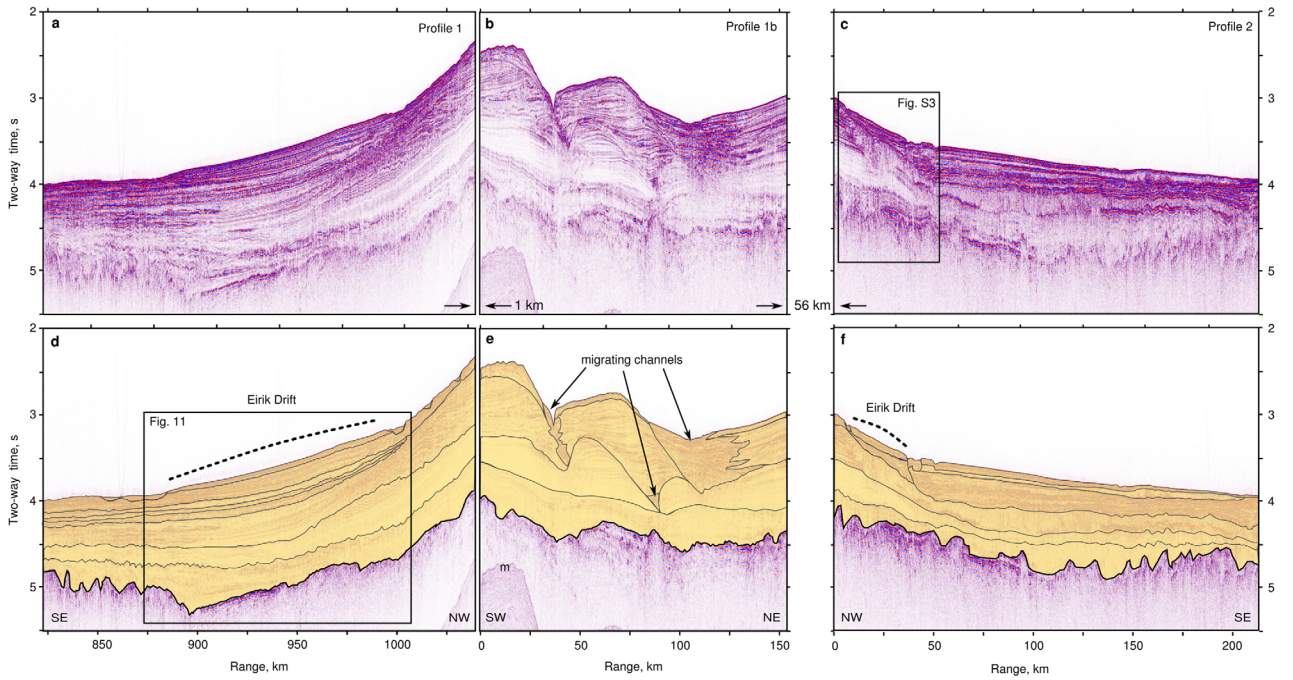

Figure 4. Portions of profiles 1, 1b, and 2, covering part of Eirik Drift (see Figure 1 for location). (a)–(c) Uninterpreted time-migrated images. (d)–(f) Geologic interpretations. Yellow shading and gray lines = sedimentary strata; dotted lines = major drift deposits; black line = sediment-basement interface; and m = water-bottom multiple reflection.

3. Björn Drift

Björn Drift was deposited as a result of deep-water current flow along the eastward-dipping bathymetric slope adjacent to the Reykjanes Ridge (Figure 1b). Björn and Gardar Drifts are probably positioned on the western side of several strands of ISOW. These drifts are separated from one another by a 200–300 m deep trough which is ~100 km wide on profile 2 (Figure 3) [*Davies and Laughton*, 1972; *McCave and Tucholke*, 1986]. The crest of Björn Drift can be tracked for 300 km, parallel to the trend of the Reykjanes Ridge. The thickest deposits along profiles 1 and 2 sit on top of 12.8 and 13.5 Myr old oceanic basement at ranges of 738 and 254 km (Figures 2 and 3, respectively). Drilling of Björn Drift at Site 114 of Deep Sea Drilling Program (DSDP) Leg 12 recovered Pleistocene and Pliocene terrigenous clayey silts [*Davies and Laughton*, 1972]. At Site 984 of Ocean Drilling Program (ODP) Leg 162, Pliocene fine-grained terrigenous sediments have been recovered [*Shipboard Scientific Party*, 1996a].

3.1. Calibration

Site 984 is located on the western side of the Iceland Basin in a water depth of 1650 m, ~12 km south of profile 2 (Figure 1a). Here, a 458 m-long continuous sequence of sedimentary core was recovered [*Jansen and Raymo*, 1996]. These sediments are dominated by fine-grained terrigenous grains, of Holocene to Pliocene (0–3 Ma) age, yielding linear sediment accumulation rates of 100–160 m Ma^{-1}.

In order to assign chronostratigraphic ages to mapped seismic horizons on profile 2, a synthetic seismogram was calculated for Site 984 (Figure 5). First, discrete sonic and density measurements from core samples (0–87 mbsf) were combined with edited sonic and bulk density logs (87–478 mbsf) to calculate a reflection coefficient series (Figures 5a–5c). Note that the discrete core measurements are noisier with larger uncertainties. Second, a source signature was estimated by stacking the direct arrival (i.e., acoustic energy that travels horizontally from the source along the streamer) from 200 shots centered at a range of 750 km on profile 2 (Figure 5d). These shots were filtered using a high-pass Butterworth filter with a cutoff frequency of 12 Hz and slope of 24 dB/octave that successfully attenuated low-frequency noise. Finally, a synthetic seismogram was calculated by convolving the estimated source signature with this reflection coefficient series with the aid of a 1.5 dimensional algorithm generously provided by Schlumberger Limited [*Schuler et al.*, 2014]. This invariant-embedded reflectivity algorithm is based upon an elastic model that computes the plane-wave response of a set of stacked layers for a point source [*Kennett*, 1983].

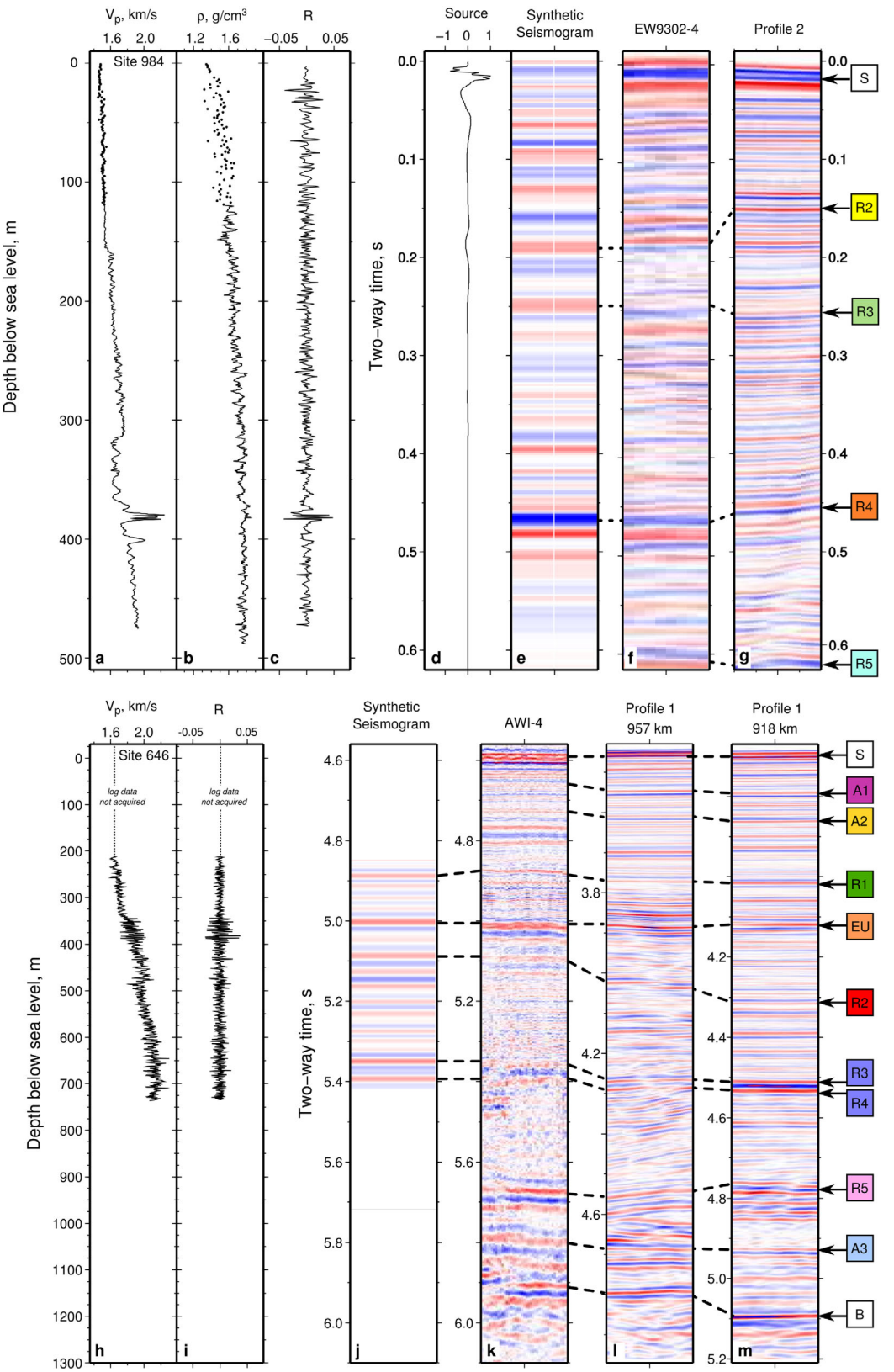
Vp, km/s
ρ, g/cm3
R
Site 984
Depth below sea level, m
Source
Synthetic Seismogram
EW9302-4
Profile 2
Two−way time, s
S
R2
R3
R4
R5
a
b
c
d
e
f
g
Site 646
log data not acquired
AWI-4
Profile 1 957 km
Profile 1 918 km
A1
A2
R1
EU
A3
B
h
i
j
k
l
m

Figure 5.

Profile 2 and Site 984 are connected by profile EW9302-4 acquired in 1996 during Cruise EW-9302 (Figure 1c) [*Shipboard Scientific Party*, 1996b]. The synthetic seismogram for Site 984 can be compared with portions of seismic reflection data from EW9302-4 and profile 2 in Figures 5f and 5g. Following the nomenclature of *Shipboard Scientific Party* [1996a], we identify three correlatable horizons. First, a bright reflection, R2, occurs at 0.15 s two-way travel time beneath the sea bed and below a series of weaker reflections. Second, R3 occurs at 0.25 s and has a series of distinctive positive reflections just above it and a series of five positive, but weak, reflections below it. Finally, a bright and positive reflection, R4, occurs at 0.45 s and corresponds to a sharp increase in velocity ($>$ 2 km s^{-1}). This layer occurs within the interval 378–383 mbsf and is identifiable on profile 2. R5 at $>$ 0.6 s was not encountered at Site 984. Nevertheless, its prominent negative polarity is recognizable. There is a minor (0.03 s) discrepancy for R2 when synthetic seismogram and profile 2 are compared. This discrepancy has several possible causes. First, well and seismic profiles are 12 km apart and stratal thickness variation may occur. Figure 6 shows the relationship between profile 2, EW9302-4 and Site 984 where thinning of the R2–R3 interval is evident. Second, the synthetic seismogram is noisy in the vicinity of R2 which hampers its identification.

3.2. Stratigraphic Framework

Our calibration strategy permits Björn Drift to be subdivided into five stratigraphic units, BJ-I to BJ-V (Figures 6 and 7 and Table 1). Reflective horizons down to R5 are subparallel with the seafloor. Beneath R5, a series of angular unconformities occur. R2 defines the base of unit BJ-I, and is the first prominent reflection beneath the seabed. Unit BJ-I appears to consist of ∼12 horizons which are subparallel with the seabed and which appear to onlap R2 at a range of 255 km on profile 1 (Figure 7n). Unit BJ-II occurs between R2 and R3 and is characterized by closely spaced, conformable reflections which are a little brighter toward the top of this unit (see Figure 5). Unit BJ-III between R3 and R4 consists of ∼15 closely spaced, weaker reflections which in places are considerably disturbed by folding and faulting (e.g., at ranges 220–230 km on profile 1; Figure 7j). An erosional surface disrupts R4 within the western portion of Björn Drift at a range of 730 km on profile 2, making identification of the base of Unit BJ-III difficult (Figure 7i). The top of Unit BJ-IV is delineated by R4 and consists of weak, lower frequency, reflections that either onlap or downlap the underlying unit. The base of Unit BJ-IV is marked by R5, which is slightly deeper than the maximum penetrated depth at Site 984. The lowermost unit, BJ-IV, consists of a number of erosional surfaces disturbed by folding and faulting, which occur between R5 and top basement. It is difficult to map with confidence conformable reflections across Björn Drift within this unit on either profile.

Chronostratigraphic ages of the four most prominent reflections identified within the sediment pile on both the well log and on the seismic profiles were determined using core recovered from Site 984. A combination of magnetic polarity events and calcareous nannofossil biostratigraphy from four boreholes at Site 984 were reported by *Shipboard Scientific Party* [1996a]. This information suggests that these sediments were deposited during Plio-Pleistocene times (∼ 3 Ma). Magnetic anomaly picks were also used to estimate the age of oceanic basement. The base of the sedimentary pile is ∼13.5 Ma beneath the thickest part of Björn Drift on profile 2 and ∼12.8 Ma on profile 1.

3.3. Drift Structure and Composition

The uppermost unit of Björn Drift comprises ∼100 m of laterally continuous, conformable reflections (Figure 7). Deposition of Björn Drift is largely continuous, uninterrupted by erosional episodes. This continuity aids correlation between profiles 1 and 2, and supports the assumption that these correlatable reflections are coeval. Unconformities toward the base of Björn Drift can be identified which have onlapping relationships above and

Figure 5. Calibration between boreholes and seismic profiles (a)–(g) Site 984; (h)–(m) Site 646. (a) P-wave velocity, V_p, as function of depth determined from core measurements (dots: depth $<$85 m) and from sonic velocity log (line: $>$89 m). (b) Gravimetric wet bulk density, ρ, from core measurements (dots: $<$119 m) and from wireline log (line: depth $>$119 m). (c) Reflection coefficient, R, calculated from V_p and ρ. (d) Source wavelet from seismic reflection experiment as function of two-way travel time. (e) Synthetic seismogram calculated by convolving source wavelet with reflection coefficient series using Schlumberger's PWTIM algorithm [*Schuler et al*., 2014]. (f) 16 seismic traces from profile EW9302-4 coincident with Site 984. (g) 40 seismic traces from profile 2 located at range 750 km. Colored boxes identify horizons following nomenclature of *Shipboard Scientific Party* [1996a]. (h) P-wave velocity, V_p, as function of depth determined from sonic velocity log [*Srivastava et al*., 1987]. (i) Reflection coefficient, R, calculated from V_p, assuming constant density. (j) Synthetic seismogram, which is a one-dimensional convolution using a 25 Hz zero-phase Ricker wavelet, including internal multiples [*Srivastava et al*., 1987]. (k) Portion of seismic line AWI-4, coincident with Site 646 [*Müller-Michaelis et al*., 2013]. (l) 40 seismic traces from profile 1, at range of 957 km (Figure 11a). (m) 40 seismic traces from profile 1, at range of 918 km (Figure 11a). Colored boxes/dashed lines identify horizons following nomenclature of *Arthur et al*. [1989] and *Müller-Michaelis et al*. [2013]. S = seabed; B = basement.

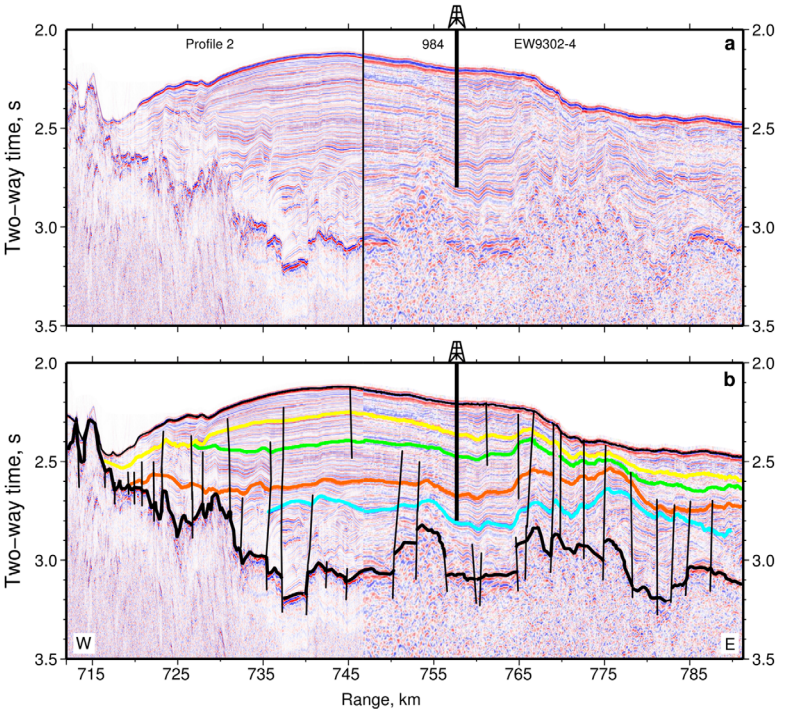

Figure 6. Stratigraphic correlation of Björn Drift between profile 2, profile EW9302-4 and Site 984 (see Figure 1 for location). (a) Portions of data from profiles 2 and EW9302-4. Vertical black line at range 747 km = intersection between profiles. (b) Interpreted version. Yellow/green/orange/blue lines = R2/R3/R4/R5 stratigraphic horizons following naming convention of *Shipboard Scientific Party* [1996a]; gray lines = faults; and black line = sediment-basement interface. See also Table 1.

erosional truncations below. In contrast to the continuous and nonerosive regime within these upper units, a more disrupted pattern of sedimentation is evident toward the base of the drift. This pattern is consistent with variable bottom current position and strength over rougher bathymetry. Pervasive normal faulting rarely shows stratigraphic growth generally dies out toward the seabed.

While a continuous sedimentary pile occurs on profile 2, Björn Drift divides into two discrete bodies separated by a basement high on profile 1 (Figure 7). Seismic reflections identified on profile 2 and calibrated with Site 984, have been correlated with the western portion of profile 1 (Figures 7c and 7d). These reflections can then be correlated eastward where R1–R5 are visible on either side of the prominent basement high which represents the crest of a VSR (Figures 7d–7h) [see *Parnell-Turner et al.*, 2014 for further details). Reflections within Björn Drift on profile 2 and on the western portion of profile 1 are laterally continuous and have a uniform frequency content. This pattern of disrupted reflections is suggestive of an erosive environment to the east of the basement high. In contrast, these currents may have a more stable locus within the trough further west. This confinement probably gave rise to more continuous strata on profile 2 and at the western end of profile 1.

The crest of the Björn Drift has migrated westward with time. The locus of maximum thickness can be used to infer how rapidly migration has taken place (Figure 7i). On profile 2, deposition migrated in a step-wise fashion during deposition of Units BJ-III to Unit BJ-I. During deposition of Unit BJ-III between 2.6 and 2.15 Ma, the drift stepped westward by ~7 km. While Unit BJ-II was deposited between 2.15 and 0.5 Ma, the drift only migrated by 1 km. Between 0.5 Ma and the present day, the drift migrated westward by 2.8 km. Given a half-spreading rate of 1 cm yr^{-1}, we expect that the position of the drift gradually shifted 5 km eastward with respect to the crest of the Reykjanes Ridge [*Searle et al.*, 1998].

4. Gardar Drift

Gardar Drift sits in the middle of the Iceland Basin, where it forms an asymmetric ridge that extends over 1000 km from the Iceland Rise in the northeast to the Charlie-Gibbs Fracture Zone in the southwest (Figure 1b). This drift is penetrated by boreholes at Sites 115, 611, and 983. It consists of nannofossil ooze

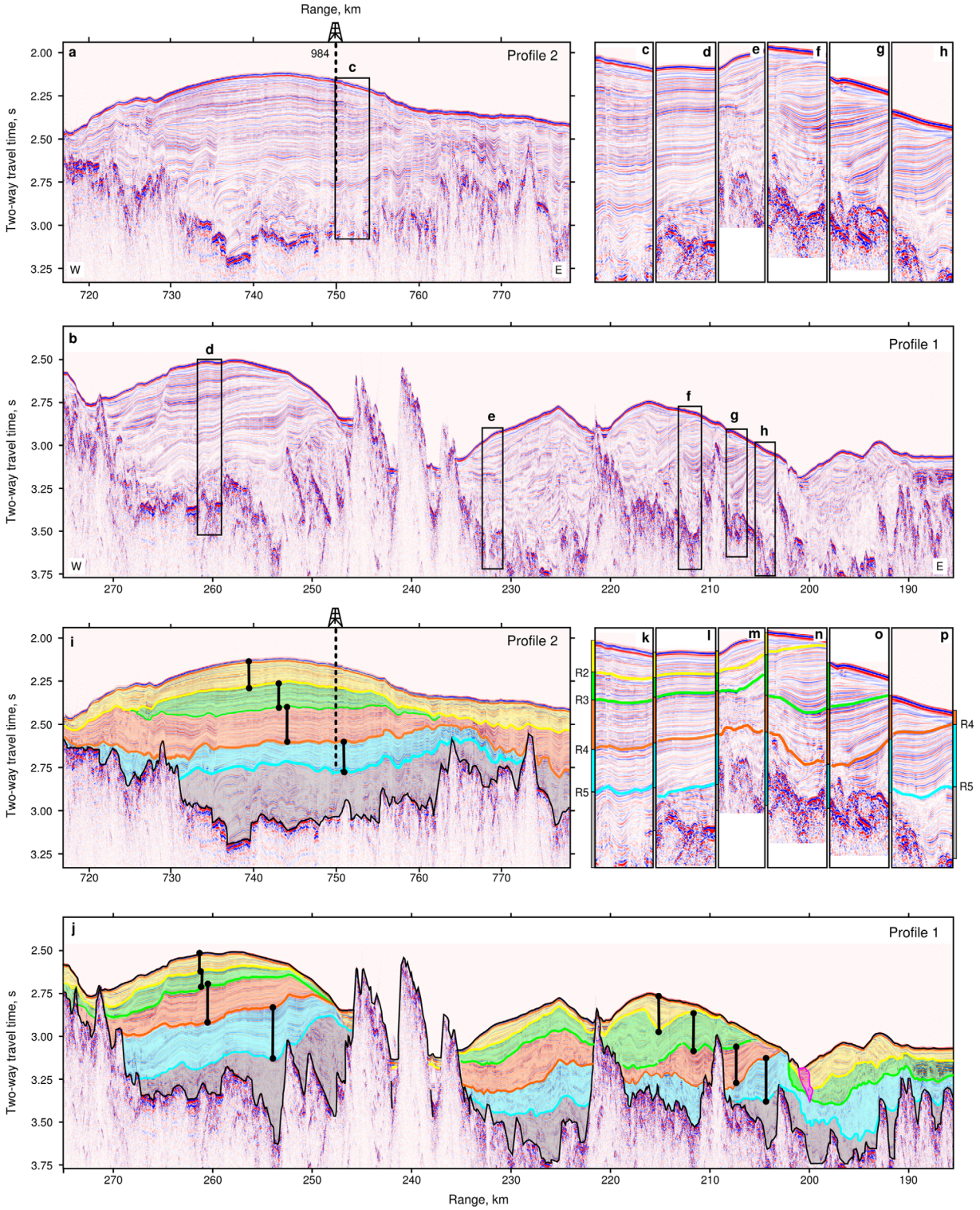

Figure 7. Stratigraphic correlation and accumulation of Björn Drift on profiles 1 and 2 (located on Figure 1). (a) Portion of profile 2. Dashed line = projected location of Site 984. (b) Portion of profile 1. (c)–(h) Strips from profiles 1 and 2 used to correlate horizons identified at Site 984. (i–p) Interpreted versions. Yellow/green/orange/blue lines = R2/R3/R4/R5 stratigraphic horizons; Black circles/lines = locus of maximal sediment thickness used in accumulation rate and drift migration estimates.

and terrestrial clastic deposits [*Shipboard Scientific Party et al.*, 1972; *Ruddiman et al.*, 1987; *Shipboard Scientific Party*, 1996b]. Deposition is thought to have started in late Miocene times. At Site 983 of ODP Leg 162, fine-grained terrigenous Pliocene sediments were recovered. At Site 115 of DSDP Leg 12 (Figure 1a),

Table 1. Ages, Interval Velocities and Solid Accumulation Rates for Björn, Gardar and Eirik Drifts[a]

Seismic unit	Basal reflection	Age range, Ma	V_{int} m s^{-1}	Maximal thickness, m			Solid acc. rate, m Ma^{-1}
				Profile 2	Profile 1 east	Profile 1 west	
Björn Drift							
BJ-I	R2	0.00–0.47	1540	119	158	79	100 ± 34
BJ-II	R3	0.47–2.15	1560	111	179	73	31 ± 15
BJ-III	R4	2.15–2.63	1630	170	165	179	163 ± 2
BJ-IV	R5	2.63–3.70	1760	155	220	268	100 ± 26
Gardar Drift							
GA-II	R2	0.00–1.00	1570	-	-	-	-
GA-III	R3	1.00–1.25	1600	-	-	-	-
Eirik Drift							
SUI-a	AI	0.0–0.8	1540	-	-	70	31
SUI-b	A2	0.8–1.4	1600	-	-	40	25
SUI-c	R1	1.4–2.5	1650	-	-	120	43
SUII	EU	2.5–4.5	1700	-	-	253	56
SUIII-a	R2	4.5–5.6	1800	-	-	156	70
SUIII-b	R3/R4	5.6–7.5	2000	-	-	197	55
SUIV-a	R5	8.1–11.0	2300	-	-	273	55
SUIV-b	A3	11.0–18.0	2400	-	-	295	27

[a]Nomenclature from *Shipboard Scientific Party* [1996a,b], *Arthur et al.* [1989], and *Müller-Michaelis et al.* [2013]. Errors are ±1σ.

hyaloclastic sandstone, probably derived from Iceland, was recovered. Near-bottom studies show that the mud wave field on this drift was built by deposition from a 300 m thick nepheloid layer (Figure 1b) [*McCave et al.*, 1980; *Bianchi and McCave*, 2000]. These studies also conclude that fine-grained sediment is carried onto the drift by an eastern strand of the major ISOW flow. The ultimate source of this sediment is probably material eroded from the slope east of Reykjanes Ridge and from the South Iceland Rise [*McCave et al.*, 1980].

Profile EW9302-3 intersects Site 983 and profile 1, permitting correlation of reflections across the drift (Figure 8). On profiles 1 and 2, the entire drift is imaged down to the top of oceanic basement which formed at 28 Ma (Figure 9). The sediment-basement interface is marked by a bright reflection, demonstrating that this drift is ~1.2 km thick. Five internal reflections identified by *Shipboard Scientific Party* [1996b] can be mapped on EW9302-3 and on profiles 1 and 2. On profile 1, the seismic character of Gardar Drift is obscured by normal faulting. At depth, the rugged oceanic basement is disrupted by fracture zone faults with throws of at least 10–25 m (Figures 1c and supporting information S5a).

Thicknesses of drift units were estimated by converting two-way travel times into depth using the average velocity of each unit documented in Table 1. These velocities are based upon information from sites 983 and 984. The youngest unit of the drift is 100 m thick on each profile and is characterized by laterally continuous reflections (Figure 9). The next unit is 200 m thick at the center of profile 1 and up to 450 m thick on profile 2. This unit thins westward and lies unconformably over two packages of older sediments which are truncated by erosional surfaces (Figure supporting information S5c). A third unit is 200 m thick on profile 1 and up to 750 m thick on profile 2. On profile 1, this unit is acoustically opaque but on profile 2 it is characterized by bright reflections which thicken eastward. At the eastern end of profile 2, this unit rests on oceanic basement. The lowest portion of the sedimentary pile consists of subparallel reflections which onlap basement. This unit is displaced by numerous basement-penetrating normal faults. However, only a small number of these faults cut through the entire section: most of them clearly terminate within the sedimentary pile. Few faults manifest stratigraphic growth, which suggests that this normal faulting post dates drift deposition.

4.1. Migrating Channels and Sedimentary Waves

At a range of 925 km on profile 2, the eastern end of Gardar Drift is bounded by a distinctive channel that can be mapped from the sea bed to 3.75 s TWTT (Figure 9c). This channel is 20–30 km wide and, assuming that it runs perpendicular to the profile, has migrated 10–20 km westward in the last 1.25 Ma (i.e., since R3). A westward migration of 0.8–1.6 cm/yr is broadly consistent with the half spreading rate of the lithospheric plate (1.25 cm/yr). The base of this channel sits between two basement highs, which suggest that these highs guided pathways of deep water flow during the early stages of drift growth.

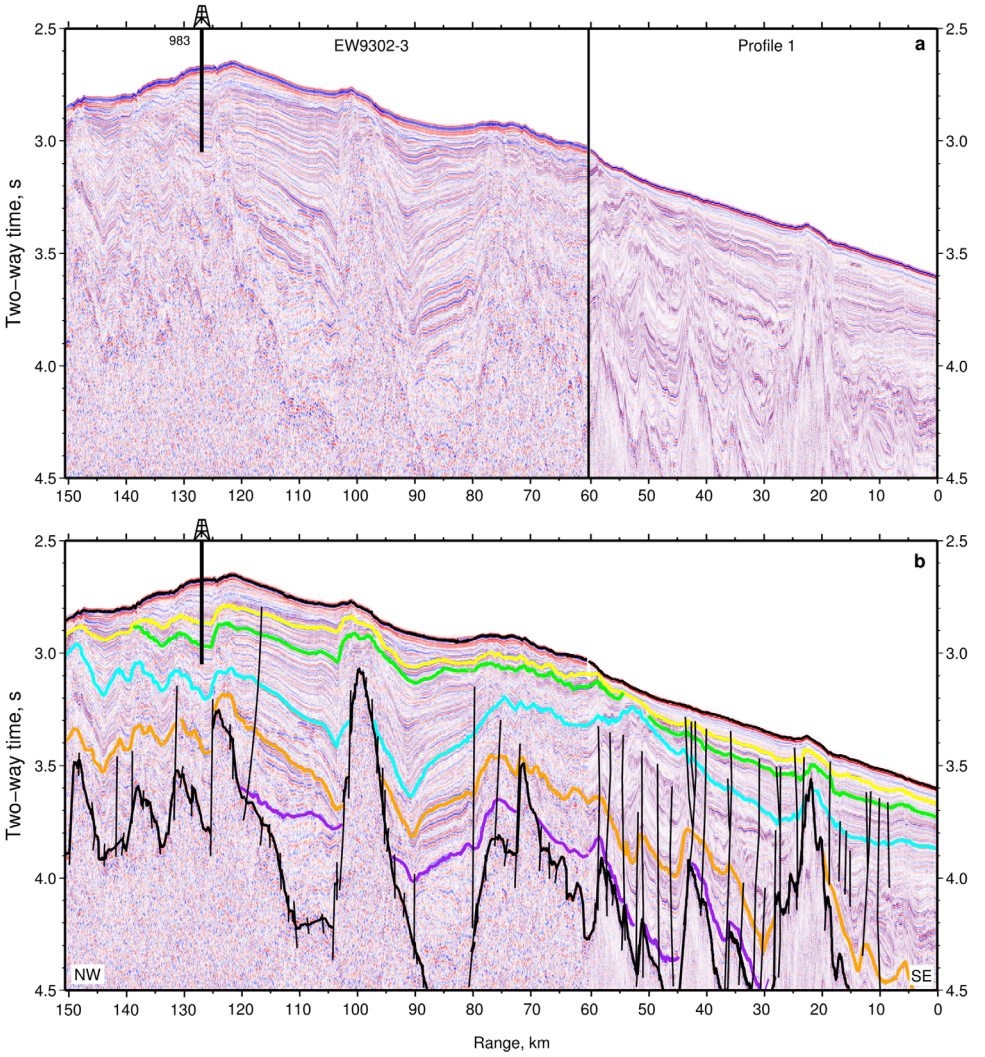

Figure 8. Stratigraphic correlation of Gardar Drift between Site 983, profile EW9302-3 and profile 1 (see Figure 1c for location). (a) Portions of data from EW9302-3 and profile 1. Vertical black line at 60 km range = intersection between profiles. (b) Interpreted version. Yellow/green/blue/orange/purple lines = R2/R3/R4/R5/R6 stratigraphic horizons, following naming convention of *Shipboard Scientific Party* [1996b]; gray lines = faults; black line = sediment-basement interface.

We expect mudwave generation to occur during the decreasing stage of the flow for flow velocities of $u \leq 0.3$ m s^{-1} [*McCave and Tucholke*, 1986; *Flood*, 1988; *Roberts and Kidd*, 1979; *Manley and Caress*, 1994; *Howe*, 1996]. West of the channel, a series of asymmetric sinusoidal waves are visible at, and just below, the sea bed (Figures 9c, 10, and supporting information S5e). The wavelength and amplitude of these waves decrease in the upslope direction. Larger waves have a peak-to-trough amplitudes of 25 m and profile-parallel wavelengths of 1 km. On the upper slopes, smaller waves occur with amplitudes of 10 m and wavelengths of 600 m. Both geometries are consistent with aggradational sedimentary waves generated by turbidity currents. They are less likely to have been generated by soft sedimentary deformation (e.g., creep folds) [*Wynn and Stow*, 2002]. Amplitudes of larger mudwaves appear to grow from 10 m at depths of ~200 mbsf to 25 m at the seabed (supporting information Figure S5f). An underlying 250 m thick package has similar wave-like characteristics. Localization of these mudwaves within a zone of turbidity current influence suggests that they are due to a turbidity current flowing down the channel. There are no mudwaves higher up slope, where they would be expected if due to thermohaline flow. Thus the channel was probably carved out by a combination of a strand of ISOW deep-water flow and sporadic turbidity currents.

At the bankfull flow stage (i.e., when levee tops correspond to the upper flow surface) then the difference in height between levees on each side of this channel can be used to determine the cross-channel slope of

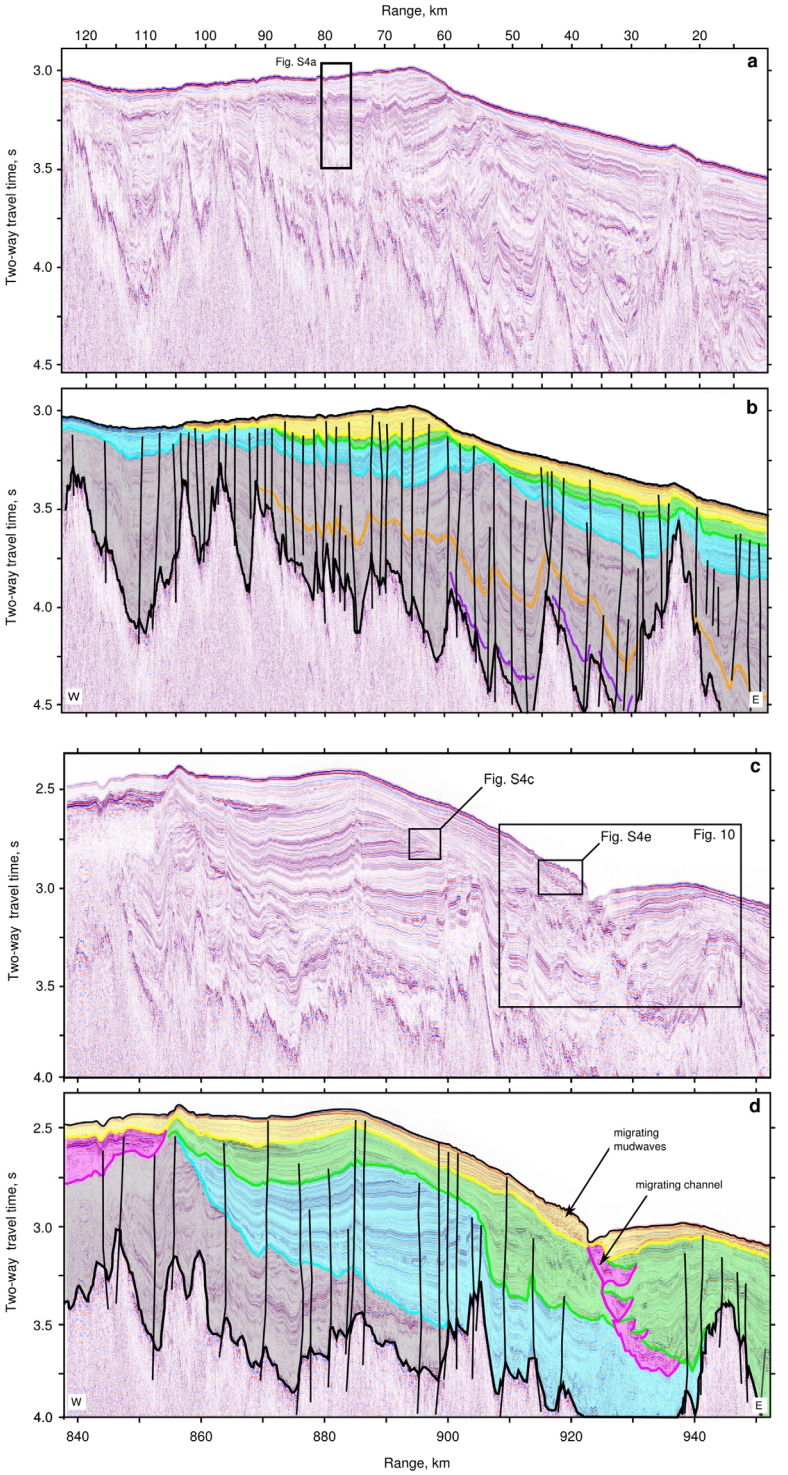

Figure 9. Sesimic profiles over Gardar Drift (see Figure 1c for locations). (a) Portion of profile 1. (b) Interpretation. Yellow/green/blue/orange/purple lines = R2/R3/R4/R5/R6 stratigraphic horizons; gray lines = faults; black line = sediment-basement interface. (c) Portion of profile 2. (d) Interpretation; pink shaded regions = channels.

the current interface (Figure 10) [*Komar*, 1969]. This slope can be used to estimate flow velocity of the turbidity current contained within the channel. Regional bathymetric maps show that this channel is nearly straight and oriented north-south. Hence the balance between Coriolis and centrifugal forces arising from the cross-channel surface slope is given by

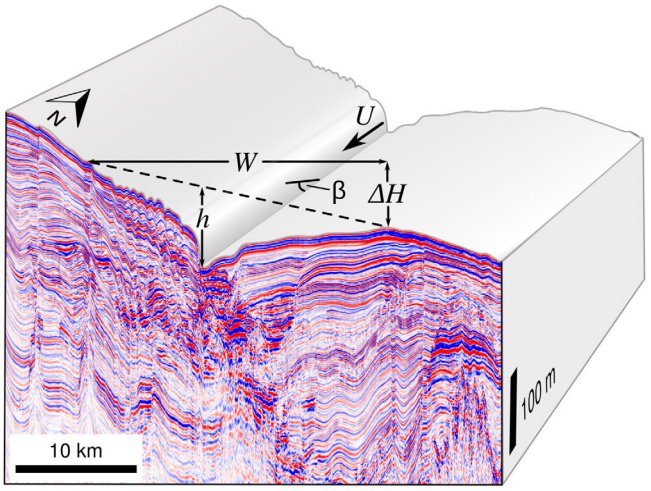

Figure 10. Cut-away image of profile 2 with parameters used in turbidity flow velocity analysis (see Figure 9c for location). U = current flow velocity; ΔH = difference in height between levees; W = channel width; and sin β = bottom slope for small β.

$$2\Omega U \sin\theta = g\left[\frac{\rho_t - \rho}{\rho_t}\right]\frac{\Delta H}{W} \quad (1)$$

where $\Omega = 7.27 \times 10^{-5}$ rad s^{-1} is the angular velocity of Earth's rotation, U is flow velocity, $\theta = 60°$N is latitude, $g = 9.81$ m^2 s^{-1} is gravitational acceleration, ρ_t is density of the turbidity current, and $\rho = 1.039$ Mg m^{-3} is density of ambient water for modern salinity of 34.96 g L^{-1}, temperature = 2.6°C and depth = 2440 m. $\Delta H = 100$ m is the difference in levee height and $W = 25$ km is channel width [*Komar*, 1969]. Current flow is driven by the down-slope component of the excess density due to suspended sediment, which is balanced by bottom and upper interfacial drags [*Middleton*, 1966]. In steady state, this force balance can be expressed as

$$\left[\frac{\rho_t - \rho}{\rho_t}\right] gh\frac{\sin\beta}{U^2} = (1+\alpha)C_0, \quad (2)$$

where $h = 140$ m is flow thickness, $\sin\beta = 2 \times 10^{-3}$ is an approximation of the along-channel slope, $\alpha = 0.5$ is the ratio between drag at the water interface and drag at the bottom of the current, and $C_0 = 0.003$ is the drag coefficient [*Ippen and Harleman*, 1952]. By eliminating density terms in equations (1) and (2), we obtain

$$U = \frac{2\Omega W h \sin\theta \sin\beta}{(1+\alpha)C_0\Delta H}. \quad (3)$$

Our estimate for peak flow velocity is 1.96 m s^{-1}. This value corresponds to $\rho_t = 1.045$ Mg m^{-3}, which is equivalent to a sediment concentration of 10.6 kg m^{-3} consistent with a moderate-sized turbidity current.

5. Eirik Drift

Eirik Drift consists of an elongate, mounded contourite deposit that is plastered along the East Greenland margin (Figure 1b). The western ends of profiles 1 and 2 traverse this drift at two positions separated by 200 km (Figures 1b and 4). Profile 1b connects these two dip lines (supporting information Figure S4). The main part of the drift was deposited by the Western Boundary Undercurrent (WBUC) during Pliocene and Pleistocene times, although deposition may have commenced as long ago as 19 Ma [*Srivastava et al*., 1987; *Hunter et al*., 2007; *Müller-Michaelis et al*., 2013; *Müller-Michaelis and Uenzelmann-Neben*, 2014]. Our analysis of this drift builds upon and complements detailed mapping of the main drift body located further to the south [*Müller-Michaelis et al*., 2013; *Müller-Michaelis and Uenzelmann-Neben*, 2014].

We note in passing that the existence of a sedimentary accumulation, known as the Snorri or West Reykjanes Drift, has been inferred from several seismic profiles [*Egloff and Johnson*, 1979; *Stow and Holbrook*, 1984]. This putative drift occurs in the northeastern quadrant of the Irminger Basin at the foot of the Iceland Rise (Figure 1b). Although a deep boundary current does flow northeastward along the western flank of the Reykjanes Ridge, our profiles suggest that this drift does not exist as far south as 62°N (supporting information Figure S1) [*McCartney*, 1992]. Instead, Snorri Drift is confined to the foot of the SW Iceland rise, as shown in Figure 1b.

5.1. Calibration

Site 646 of ODP Leg 105 is located 625 km south of the intersection between profiles 1 and 1b in 3450 m of water (Figure 1). This borehole recovered 767 m of predominantly fine-grained terrigenous Miocene (8.6 Ma)

sediments [*Srivastava et al*., 1987]. The linear sediment accumulation rate for this drilled section is 90 m Ma^{-1}. A synthetic seismogram calculated by *Srivastava et al*. [1987] was used for calibration (Figure 5j). This seismogram was calculated from a sonic velocity log which spans 205–740 mbsf. A density log was not acquired and *Srivastava et al*. [1987] used an unspecified density to calculate acoustic impedance as a function of depth. The calculated impedance function was then convolved with a 25 Hz zero-phase Ricker wavelet. The resultant seismogram includes internal multiple waves.

Following *Müller-Michaelis et al*. [2013], this synthetic seismogram is correlated to seismic profile AWI-20090004 (referred to here for convenience as AWI-4; Figure 5k). This profile intersects Site 646, south Cape Farewell (Figure 1b). We matched prominent reflections on the synthetic seismogram and on profile AWI-4 with profile 1 (Figures 5l and 5m). We acknowledge that this correlation, which is primarily based upon seismic character, is necessarily preliminary since these locations are separated by 625 km. For consistency, the stratigraphic nomenclature of *Srivastava et al*. [1987] and *Müller-Michaelis et al*. [2013] is used (note that labeled reflections, for example R1 and R2, do not imply any correlation with similarly labeled reflections on Björn or Gardar Drifts).

We identified 10 correlatable reflections. A1 and A2 occur at 0.08 and 0.12 s beneath the seabed on both AWI-4 and profile 1. R1 occurs at 4.02 s on profile 1 and is the first reflection that can be confidently correlated between Site 646, AWI-4 and profile 1. EU is a bright reflection that represents an erosional unconformity which truncates underlying strata (Figure 11). R2 is the shallowest of a sequence of bright sub-parallel reflections which occur above an interval of weak reflectivity. R3 and R4 at 4.51 s on profile 1 are subparallel reflections identified toward the bottom of Site 646 and at 5.48s on AWI-4. R5 is a prominent peak-trough-peak triplet that marks the top of a zone of bright reflectivity, matching what is seen on AWI-4. At the base of the stratigraphic pile, A3 is a strong event at 4.92 s on AWI-4 and on profile 1. Finally, a basement reflection is tentatively identified on both profiles.

5.2. Structure and Stratigraphy

The existence of drift sediments on the continental slope in profiles 1 and 2 suggests that Eirik Drift extends 650 km north of Cape Farewell where it has been studied in greater detail [e.g., *Clausen*, 1998; *Rasmussen et al*., 2003]. On profile 1, the drift has a maximum thickness of ~1300 m. At its proximal northern end, Eirik Drift can be divided into four units (SU-I–SU-IV; Figure 11 and Table 1). The uppermost unit, SU-I, consists of cycles of conformable, bright reflections that are subparallel to the seabed. SU-I is bounded to the east and west by a pair of distinctive channels that are 5 and 10 km wide, respectively. These channels are clearly visible at ranges of 890 and 990 km on profile 1 (Figure 11b). Biostratigraphic constraints at Site 646 suggest that R1 is 2.5 Ma at the base of SU-I [*Arthur et al*., 1989].

SU-II consists of a set of subparallel reflections whose amplitudes diminish toward the margin. Asymmetric mud waves are visible toward the center of this unit at a range 930 km (Figures 11 and 12b). These mud waves have wavelengths of $<$1 km and amplitudes of 15–20 m. Their sense of asymmetry indicates upslope migration. The base of SU-II is marked by an erosional unconformity, EU, that occurs at ~5 s TWTT at Site 646 where it has been assigned an age of 4.5 Ma (Figure 5m). Beneath unconformity EU, strata are truncated at 980–1100 km along profile 1.

In its upper part, SU-III is distinguished either by weak reflections or by an acoustically transparent layer. A similar character has been described within the main body of Eirik Drift near Site 646 [*Arthur et al*., 1989; *Hunter et al*., 2007; *Müller-Michaelis et al*., 2013; *Müller-Michaelis and Uenzelmann-Neben*, 2014]. The base of SU-III is marked by R3 and R4, which are seen at Site 646. Both reflections can also be identified at 4.51 s on profiles AWI-4 and 1 (Figure 5m). SU-IV is characterized by a bright reflection, labeled R5, at its base. This reflection is visible at 4.78 s on Figure 5m.

The seismic character of each unit is summarized in Figure 12. Despite the distance between profile 1 and Cape Farewell, our summary is in agreement with the analysis of *Arthur et al*. [1989] from Site 646. For example, the generally weaker reflections of SU-IV are overlain by brighter parallel reflections of SU-III which suggests that a similar change in current flow regime occurred at both locations. Other features can be identified, such as the distinctive acoustically transparent unit between R2 and EU as well as the dipping reflections, migrating mudwaves, and erosional surfaces of SU-II. A commonality of current-related sedimentary features at Cape Farewell and on profile 1 implies that regional changes in flow regime have affected

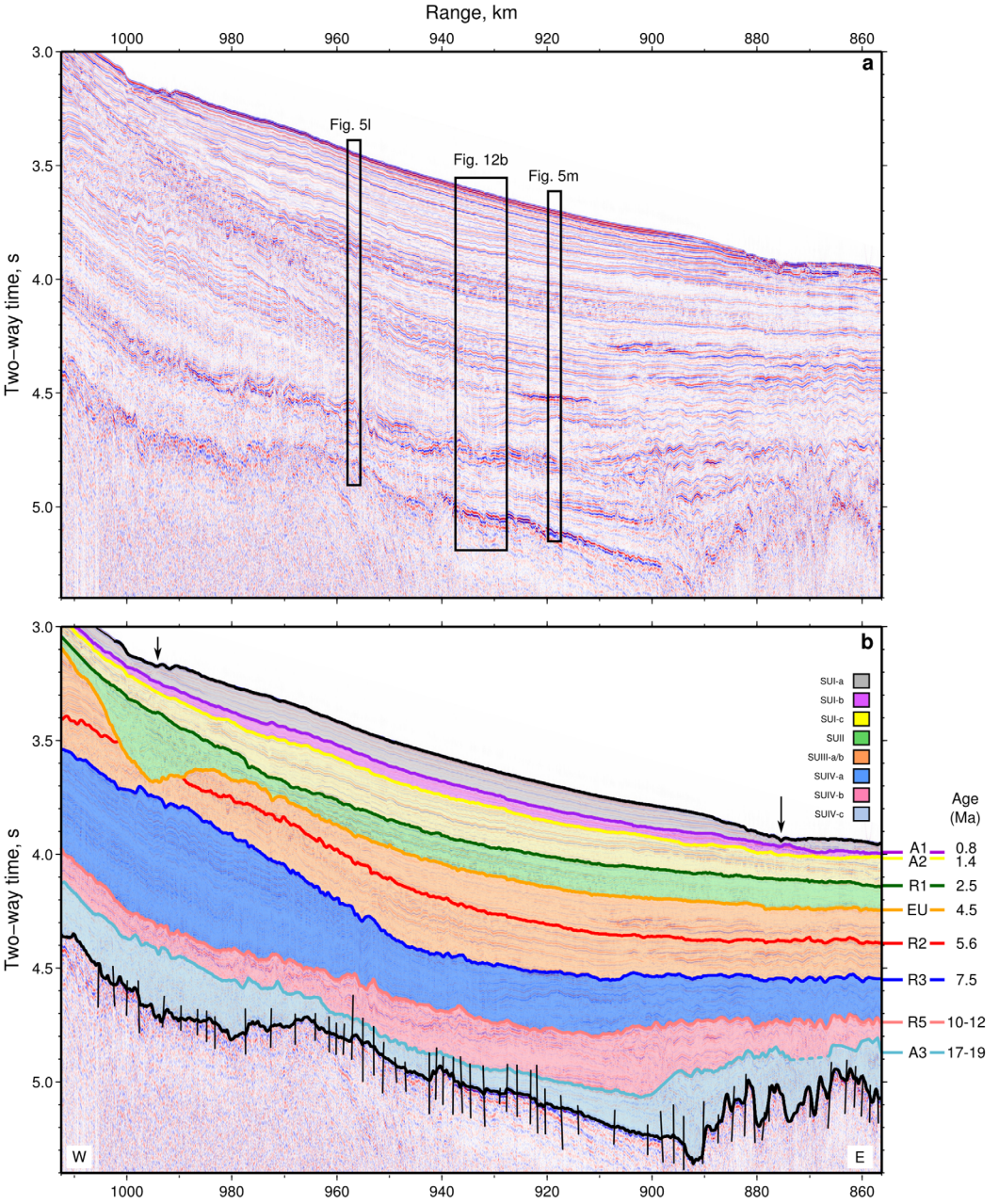

Figure 11. Portion of profile 1 which crosses Eirik Drift (see Figure 1c for location). (a) Uninterpreted time-migrated image. (b) Interpretation. Colored lines = interpreted horizons with ages noted; colored intervals = stratigraphic units; upper/lower black lines = seabed/basement reflections, respectively; arrows = bounding channels.

drift accumulation [*Clausen*, 1998; *Hunter et al.*, 2007; *Rasmussen et al.*, 2003; *Müller-Michaelis et al.*, 2013; *Müller-Michaelis and Uenzelmann-Neben*, 2014].

6. Solid Sediment Accumulation History

Since porosity varies as a function of depth, it is important to calculate solid sediment accumulation rates for Björn and Eirik Drifts (i.e., remove the effects of porosity which varies as a function of depth). The solid sediment accumulation rate is the linear sedimentation rate reduced by porosity. First, a history of maximum sedimentary thicknesses was selected for each drift using age constraints based upon Sites 984 and 646. We assume that the variation of porosity, ϕ, as a function of depth, z, is described by

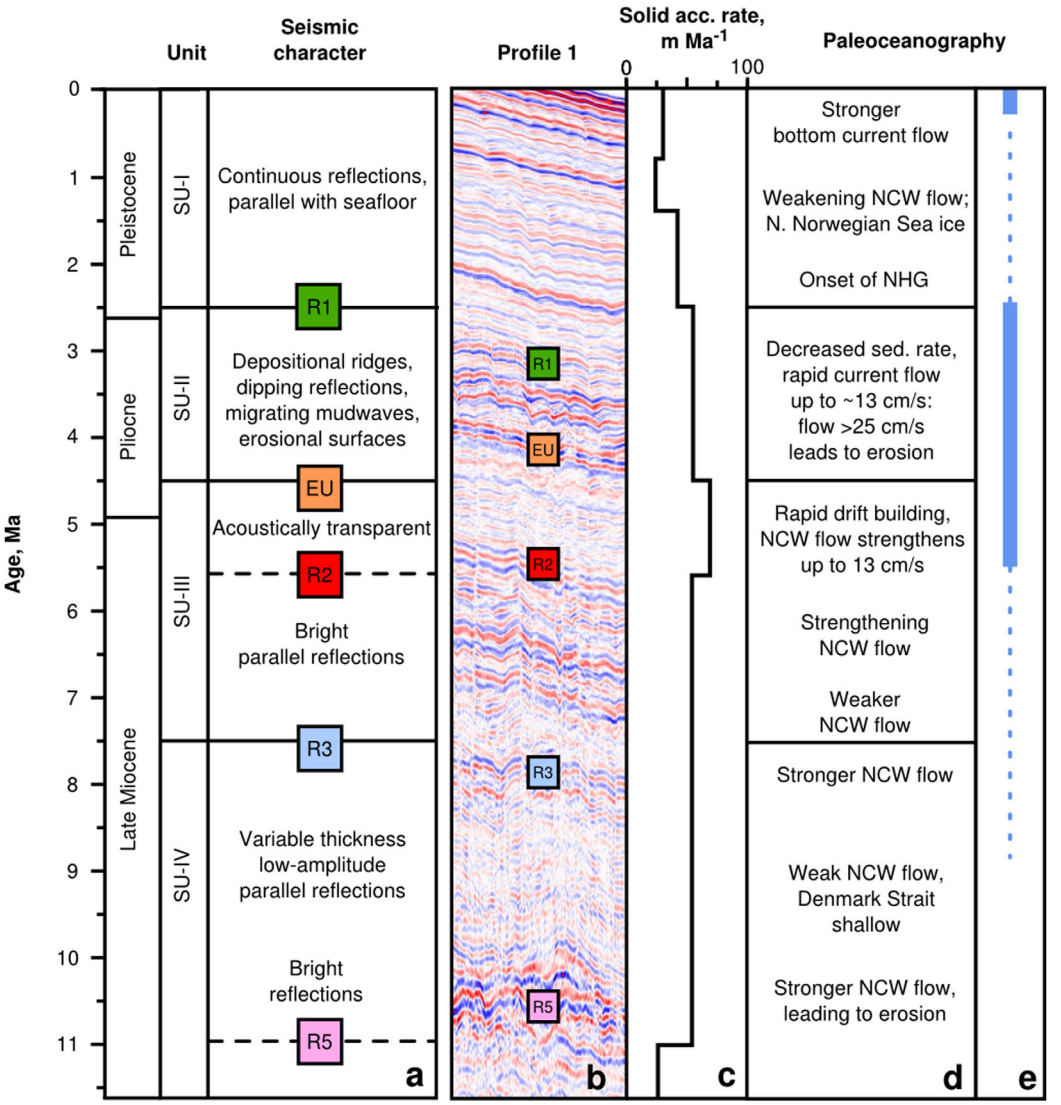

Figure 12. Seismic character and paleoceanographic history of Eirik Drift since late Miocene times. (a) Characteristics of major seismic units [*Hunter et al.*, 2007; *Müller-Michaelis et al.*, 2013; *Müller-Michaelis and Uenzelmann-Neben*, 2014]. (b) Portion of profile 1, major reflections labeled. Location shown in Figure 11. (c) Solid sedimentation rate calculated from Site 646 and profile 1. (d) Paleoceanographic events. (e) Thick/dotted lines = strong/weak bottom currents [*Hunter et al.*, 2007].

$$\phi(z)=\phi_{\circ}\exp\left(-z/\lambda\right) \tag{4}$$

where $\phi_{\circ}$ is the initial porosity and λ is the compaction decay length. We estimate the optimal values of $\phi_{\circ}$ and λ using porosity measurements from Sites 984 and 646 (supporting information Figure S6). At Site 984, we obtained $\phi_{\circ}=0.62$ and $\lambda=2.4$ km and at Site 646 we obtained $\phi_{\circ}=0.66$ and $\lambda=2.1$ km. The solid thickness, z_s, is given by

$$z_s=z_2-z_1+\phi_{\circ}\lambda[\exp\left(-z_2/\lambda\right)-\exp\left(-z_1/\lambda\right)] \tag{5}$$

where z_1 and z_2 are depths to top and base of a given layer, respectively. The resultant solid accumulation rates for both drifts are summarized in Table 1.

7. Discussion

Analysis of contourite drift deposition can be used to test the hypothesis that varying dynamic support beneath major oceanic gateways has influenced ancient oceanic circulation within the North Atlantic Ocean. There is

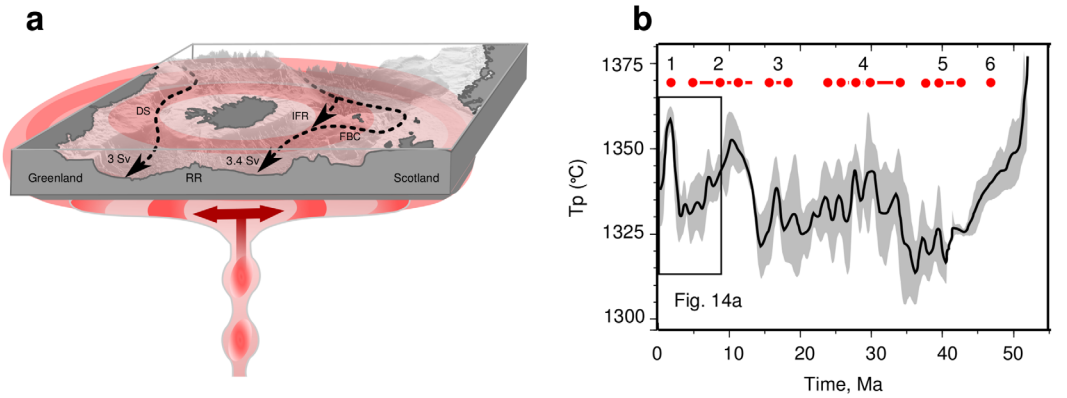

Figure 13. (a) Cartoon showing relationship between Iceland mantle plume and deep-water circulation. Dashed lines = deep overflow water [*Hansen and Østerhus*, 2000; *Olsen et al.*, 2008]; pink disk/stem = idealized extent of Iceland plume and plume head; darker pink blobs = thermal anomalies; DS = Denmark Strait; RR = Reykjanes Ridge; IFR = Iceland-Faroe Ridge; FBC = Faroe Bank Channel. (b) Mantle potential temperature (T_p) at the Denmark Strait calculated from V-shaped ridges for past 55 Ma [*Parnell-Turner et al.*, 2014]. Numbered red circles/lines = sets of V-shaped ridges.

evidence that thermal perturbations are generated within the conduit that feeds the Icelandic plume [*Parnell-Turner et al.*, 2014]. These perturbations appear to be advected horizontally beneath the thickening lithospheric plate, causing transient uplift and subsidence of the Denmark Strait and Iceland-Faroe Ridge (Figure 13a). The history of dynamic support inferred from V-shaped ridges south of Iceland provides a framework into which we can place observations of sediment accumulation rates and inferred average current strength over time (Figure 13b).

There is a reasonable correspondence between the record of potential temperature, T_p, which plays a role in controlling regional dynamic support, and %NCW overflow (Figure 14). Between 6 Ma and 2.5 Ma, the plume was relatively cool with T_p of ~1335°C. During this period, %NCW was elevated which suggests that both the Denmark Strait and the Iceland-Faroe Ridge were deeper. Between 2.5 and 0.5 Ma, T_p increased to ~1355°C and dynamic support beneath these two oceanic gateways was greater by ~200 m. During this period, %NCW was reduced, which suggests that uplift of both gateways inhibited deep-water flow into the North Atlantic Ocean. Over the last 0.5 Ma, T_p has decreased and %NCW has increased, consistent with renewed deep-water overflow. These inferred bathymetric controls are corroborated by the results of fully coupled oceanic-atmospheric numerical experiments [*Robinson et al.*, 2011].

7.1. Late Miocene–Early Pliocene Times (6.0–2.5 Ma)

A decrease in mantle potential temperature, T_p, and elevated %NCW between 6 and 2.5 Ma was accompanied by rapid accumulation of sediment at both Björn and Eirik Drifts (Figure 14). Accumulation of Björn Drift has a maximum rate of ~160 m Ma^{-1} at ~2.5 Ma. Accumulation rates of ~60 m Ma^{-1} have been recorded at Eirik Drift near Cape Farewell [Site 646 and seismic profiles; *Srivastava et al.*, 1987; *Müller-Michaelis and Uenzelmann-Neben*, 2014]. A similar sedimentation rate was estimated 625 km further north on profile 1. This agreement suggests that the rate of accumulation of Eirik drift is controlled over hundreds of kilometers and was moderated by deep-water currents. This period of elevated sedimentation rate coincides with deposition of mud waves which occur within SU-II on profile 1 and at Cape Farewell. These waves are indicative of flow rates $\geq$13 cm s^{-1} (Figure 12) [*Flood*, 1988]. Changes in benthic foraminiferal assemblages, which coincide with a bright basal reflection, suggest that more vigorous circulation occurred at this time [*Arthur et al.*, 1989; *Hunter et al.*, 2007]. In addition to reduced dynamic support beneath the Denmark Strait and the Iceland-Faroe Ridge, NCW flow may have been intensified under warmer conditions and a more vigorous AMOC which immediately preceded Pliocene cooling. In this way, locus of NCW formation and its subsequent flow paths caused Eirik Drift to accumulate along the primary sediment dispersal route which triggered an increase in drift building rate [*Müller-Michaelis and Uenzelmann-Neben*, 2014].

7.2. Northern Hemisphere Glaciation

Onset of Northern Hemisphere Glaciation took place during late Pliocene times (i.e., 3 Ma) [*Maslin et al.*, 1998; *Bartoli et al.*, 2005]. Progressively increasing amounts of ice-rafted debris and synchronous ice sheet development in Greenland, Scandinavia, and North America have been documented at 2.72–2.75 Ma

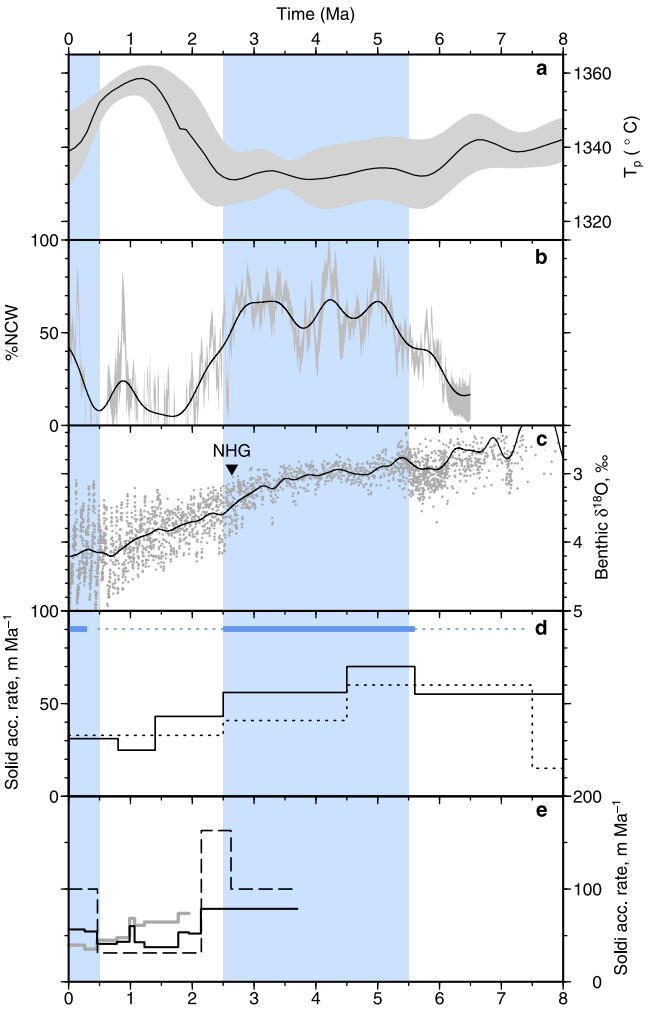

Figure 14. Mantle potential temperature (T_p), northern Component Water overflow (%NCW) and drift accumulation through time. Blue bands = periods when Iceland plume was cooler. (a) Black line with error band = T_p at Denmark Strait [*Parnell-Turner et al.*, 2014]. (b) %NCW with error band [*Poore et al.*, 2006]. (c) Gray points = stacked deep-sea oxygen isotope record [*Lisiecki and Raymo*, 2005; *Zachos et al.*, 2001]; black line = smoothed with 0.5 Ma width Gaussian filter; triangle = onset of Northern Hemisphere Glaciation (NHG) [*Kleiven et al.*, 2002]. (d) Solid sedimentation rate of Eirik Drift. Dotted black line = rate from *Müller-Michaelis and Uenzelmann-Neben* [2014]; dashed line = rate from profile 1 (Figure 11); thick/dotted blue lines = strong/weak bottom currents [*Hunter et al.*, 2007]; (e) Solid sedimentation rate of Björn drift. Black/gray lines = rate at ODP Sites 984 and 983, respectively [*Jansen and Raymo*, 1996]; dashed line = rate calculated from profiles 1 and 2 (Figure 7).

[*Kleiven et al.*, 2002]. This intensification corresponds to an increasing trend within the oxygen isotope record (Figure 14c) [*Lisiecki and Raymo*, 2005]. General circulation modeling has suggested that climatic shifts associated with closure of the Panamanian seaway, with termination of a permanent El Niño state, or with regional uplift, do not account for significant growth of the Greenland icesheet [*Lunt et al.*, 2008]. Decreasing atmospheric CO_2, from elevated mid Pliocene values to lower Quaternary values are conceivably responsible for significant increase in Greenland glaciation [*Lunt et al.*, 2008]. The reasons for this decrease in atmospheric CO_2 are unclear [*Bartoli et al.*, 2011]. Here, we suggest that restriction of deep-water flow, caused by transient uplift of the Denmark Strait and the Iceland-Faroe Ridge, may have played some role in reducing the vigor of AMOC and inhibiting production of NCW in late Pliocene times. This inhibition could have preconditioned a coupled ocean-climate system, with full glaciation triggered by variations in Earth's orbital cycles along with a decreasing trend in atmospheric CO_2.

7.3. Late Pliocene–Middle Pleistocene Times (2.5–0.5 Ma)

High values of T_p and decreased %NCW between 2.5 and 0.5 Ma coincide with lower accumulation rates of Björn and Eirik Drifts during this period (Figure 14). Solid accumulation rates of Björn fell from over 150 m Ma^{-1} to ~50 m Ma^{-1} but accumulation of Eirik Drift decreased more gradually from 60 m Ma^{-1} to ~30 m Ma^{-1}. This trend of decreasing accumulation rate is recorded at drill sites and on seismic profiles within both the Iceland and Irminger Basins. Static distribution of depocenters and absence of stratal truncations on seismic profiles close to Site 646 may indicate shallowing and weakening of NCW flow [*Müller-Michaelis and Uenzelmann-Neben*, 2014]. Upslope drift migration caused by decreasing current intensity was also noted by *Arthur et al.* [1989] and by *Hunter et al.* [2007]. Weakening of the NCW flow may have been magnified by the effects of Pliocene cooling and of Northern Hemisphere Glaciation [*Müller-Michaelis and Uenzelmann-Neben*, 2014]. Increased sea-ice cover across the Nordic seas could have shifted NCW production southward, exposing Eirik Drift to a weaker branch of NCW flow [*Müller-Michaelis and Uenzelmann-Neben*, 2014].

7.4. Middle Pleistocene–Holocene Times (<0.5 Ma)

Renewal of %NCW is corroborated by an increase in solid accumulation rate of Björn Drift at Site 984 and on seismic profiles 1 and 2 (Figure 14d). The average rate is ~100 m Ma^{-1} over the last 0.5 Ma. At Eirik Drift,

an alternation of brighter and weaker reflections within the shallowest strata are interpreted as signs of strengthening bottom current flow during glacial-interglacial cycles, although accumulation rates are uniformly low [*Hunter et al*., 2007].

Evidence for renewed NADW flow in recent times is consistent with a decrease in dynamic support beneath the Denmark Strait and the Iceland-Faroe Ridge. This decrease is manifest by the present-day location of a thermal pulse along the Reykjanes Ridge. *Parnell-Turner et al*. [2013] show that this location occurs at a distance of ~500 km from the center of the Icelandic plume. Assuming a radial planform, this pulse is expected to lie beneath lithosphere ~50–100 km beyond the two oceanic gateways. Consequently, the Denmark Strait and Iceland-Faroe Ridge are inferred to have gradually subsided over the last 0.5 Ma.

8. Conclusions

Regional seismic reflection profiles that cross the Björn, Gardar, Hatton, and Eirik Drifts are described and analyzed. Mappable reflections are correlated between profiles and calibrated using borehole data. The detailed architecture of these contourite drifts suggest that loci and rates of deposition varied through time. We have reconstructed the history of accumulation rate for Björn and Eirik Drifts. There is a good correlation between variations in dynamic support of the lithosphere, recorded by VSRs straddling the Reykjanes Ridge, and the accumulation history of Björn and Eirik Drifts [*Parnell-Turner et al*., 2014]. Periods of rapid sediment accumulation correspond to periods of reduced dynamic support. These observations match the history of NCW strength constructed from the isotope record of benthic foraminifera [*Poore et al*., 2006]. Our observations can be explained by the interaction between mantle convective circulation and uplift of the oceanic gateways either side of Iceland. Thermal anomalies, advecting through the conduit of the Icelandic mantle plume, may have triggered transient uplift of the Denmark Strait and of the Iceland-Faroe Ridge. This uplift reduces flow of NCW into the North Atlantic Ocean, which in turn controls the rate and locus of deposition of contourite drift sediment in the Iceland and Irminger Basins. We therefore suggest a causal relationship between mantle convective behavior and processes taking place at the surface. These processes may have contributed to preconditioning of the climatic system that led to onset of Northern Hemisphere Glaciation in late Pliocene times. In this way, deep mantle processes may govern long-term bathymetric configuration of oceanic basins with implications for deep-water circulation.

Acknowledgments

Seismic reflection data presented in this paper can be obtained from NW (njw10@cam.ac.uk). This work is partly supported by Natural Environment Research Council grant NE/G007632/1. R.P.T. was supported by the University of Cambridge Girdler Fund and by BP Exploration. The professionalism and dedication of the Master, crew, and science party during RRS *James Cook* cruise JC50 are warmly acknowledged. G. Uenzelmann-Neben generously provided access to seismic reflection profile AWI-20090004. We thank Schlumberger for permission to use their proprietary software and we are grateful to P. Christie and J. Schuler for help in calculating synthetic seismograms. Figures prepared with the GMT and Seismic Unix software packages [*Wessel and Smith*, 1998; *Cohen and Stockwell*, 2013]. Cambridge Earth Sciences contribution ESC.3495

References

Arthur, M. A., S. P. Srivastava, M. Kaminski, R. Jarrard, and J. Osler (1989), Seismic stratigraphy and history of deep circulation and sediment drift development in Baffin Bay and the Labrador Sea, in *Proceedings of Ocean Drilling Program, Science Results*, vol. 105, edited by S. P. Srivastava, et al., pp. 957–988, Ocean Drill. Program, College Station, Tex.

Bartoli, G., M. Sarnthein, M. Weinelt, H. Erlenkeuser, D. Garbe-Schönberg, and D. W. Lea (2005), Final closure of Panama and the onset of northern hemisphere glaciation, *Earth Planet. Sci. Lett.*, *237*, 33–44, doi:10.1016/j.epsl.2005.06.020.

Bartoli, G., B. Hönisch, and R. E. Zeebe (2011), Atmospheric CO_2 decline during the Pliocene intensification of Northern Hemisphere glaciations, *Paleoceanography*, *26*, PA4213, doi:10.1029/2010PA002055.

Bianchi, G. G., and I. N. McCave (2000), Hydrography and sedimentation under the deep western boundary current on Björn and Gardar Drifts, Iceland Basin, *Mar. Geol.*, *165*(1), 137–169.

Boyle, E. A., and L. D. Keigwin (1982), Deep circulation of the North Atlantic over the Last 200,000 Years: Geochemical evidence, *Science*, *218*, 784–787, doi:10.1126/science.218.4574.784.

Broecker, W. S., and G. H. Denton (1989), The role of ocean-atmosphere reorganizations in glacial cycles, *Geochim. Cosmochim. Acta*, *53*, 2465–2501.

Clausen, L. (1998), Late neogene and quaternary sedimentation on the continental slope and upper rise offshore southeast Greenland: Interplay of contour and turbidity processes, in *Proceedings of Ocean Drilling Program, Science Results*, vol. 152, edited by A. Saunders, H. Larsen, and S. Wise, pp. 3–18, Ocean Drill. Program, College Station, Tex.

Cohen, J. K., and J. W. Stockwell (2013), *CWP/SU: Seismic Un*x. Release No. 43R5: An Open Source Software Package for Seismic Research and Processing*, Cent. for Wave Phenomena, Colo. School of Mines.

Cunningham, A., J. A. Howe, and P. F. Barker (2002), Contourite sedimentation in the Falkland Trough, western South Atlantic, in *Deep-water Contourite Systems: Modern Drifts and Ancient Series, Seismic and Sedimentatary Characteristics, Mem*., vol. 22, edited by D. A. V. Stow et al., pp. 337–352, Geol. Soc., London, U. K.

Davies, T. D., and A. S. Laughton (1972), Sedimentary processes in the North Atlantic Ocean, edited by A. S. Laughton and W. A. Berggren, *Initial Rep. Deep Sea Drill. Proj*., 12, . 905–934.

Delorey, A., R. A. Dunn, and J. B. Gaherty (2007), Surface wave tomography of the upper mantle beneath the Reykjanes Ridge with implications for ridge-hot spot interaction, *J. Geophys. Res.*, *112*, B08313, doi:10.1029/2006JB004785.

Egloff, F., and G. L. Johnson (1979), Erosional and depositional structures of the southwest Iceland insular margin: Thirteen geophysical profiles, in *Geological and Geophysical Investigations of Continental Margins*, edited by J. S. Watkins, L. Montadert, and P. W. Dickerson, *AAPG Mem. 29*, 43–63

Faugères, J-C., D. A. V. Stow, P. Imbert, and A. Viana (1999), Seismic features diagnostic of contourite drifts, *Mar. Geol.*, *162*(1), 1–38, doi: 10.1016/S0025-3227(99)00068-7.
Flood, R. D. (1988), A lee wave model for deep-sea mudwave activity, *Deep Sea Res., Part A*, *35*(6), 973–983.
Hansen, B., and S. Østerhus (2000), North Atlantic: Nordic Seas exchanges, *Prog. Oceanogr.*, *45*, 109–208.
Howe, J. A. (1996), Turbidite and contourite sediment waves in the northern Rockall Trough, North Atlantic Ocean, *Sedimentology*, *43*, 219–234.
Hunter, S., D. Wilkinson, J. Stanford, D. A. V. Stow, S. Bacon, A. M. Akhmetzhanov, and N. H. Kenyon (2007), The Eirik Drift: A long-term barometer of North Atlantic deepwater flux south of Cape Farewell, Greenland, in *Economic and Palaeoceanographic Significance of Contourite Deposits, Geol. Soc. Spec. Publ. 276*, edited by A. Viana and M. Rebesco, pp. 245–263, Geol. Soc. of London, London, U. K., doi:10.1144/GSL.SP.2007.276.01.12.
Ippen, A. T., and R. F. Harleman (1952), Steady-state characteristics of subsurface flow, *Natl. Bur. Stand. Circ. U.S.*, *521*, 79–93.
Jansen, E., and M. E. Raymo (1996), Leg 162: New frontiers on past climates, in *Proceedings of Ocean Drilling Programs, Initial Reports*, vol. 162, edited by E. Jansen et al., pp. 5–20, Ocean Drill. Program, College Station, Tex.
Johnson, G. L., and E. Schneider (1969), Depositional ridges in the North Atlantic, *Earth Planet. Sci. Lett.*, *6*, 416–422.
Jones, S. M., N. J. White, B. J. Clarke, E. Rowley, and K. Gallagher (2002), Present and past influence of the Iceland Plume on sedimentation, in *Exhumation of the North Atlantic Margin: Timing, Mechanisms and Implications for Petroleum Exploration, Geol. Soc. Spec. Publ. 196*, edited by A. G. Dore, et al., pp. 13–25, Geol. Soc. of London, London, U. K.
Jones, S. M., B. J. Murton, J. G. Fitton, N. J. White, J. Maclennan, and R. Walters (2014), A joint geochemical-geophysical record of time-dependent mantle convection south of Iceland, *Earth Planet. Sci. Lett.*, *386*, 86–97, doi:10.1016/j.epsl.2013.09.029.
Kellogg, T. B. (1980), Paleoclimatology and paleo-oceanography of the Norwegian and Greenland Seas: The last 450,000 years, *Boreas*, *9*, 115–137.
Kennett, B. L. N. (1983), *Seismic Wave Propagation in Stratified Media*, Cambridge Univ. Press.
Khélifi, N., M. Sarnthein, N. Andersen, T. Blanz, M. Frank, D. Garbe-Schönberg, B. A. Haley, R. Stumpf, and M. Weinelt (2009), A major and long-term Pliocene intensification of the Mediterranean outflow, 3.5-3.3 Ma ago, *Geology*, *37*(9), 811–814, doi:10.1130/G30058A.1.
Kleiven, H. F., E. Jansen, T. Fronval, and T. M. Smith (2002), Intensification of Northern Hemisphere glaciations in the circum Atlantic region (3.5-2.4 Ma): Ice-rafted detritus evidence, *Palaeogeogr. Palaeoclimatol. Palaeoecol.*, *184*, 213–223.
Koenitz, D., N. J. White, I. N. McCave, and R. Hobbs (2008), Internal structure of a contourite drift generated by the Antarctic Circumpolar Current, *Geochem. Geophys. Geosyst.*, *9*, *Q06012*, doi:10.1029/2007GC001799.
Komar, P. D. (1969), The channelized flow of turbidity currents with application to Monterey Deep-Sea Fan Channel, *J. Geophys. Res.*, *74*(18), 4544–4558.
Laberg, J., K. Dahlgren, and T. Vorren (2005), The Eocene-late Pliocene paleoenvironment in the Voring Plateau area, Norwegian Sea—paleoceanographic implications, *Mar. Geol.*, *214*(1-3), 269–285, doi:10.1016/j.margeo.2004.10.031.
Lisiecki, L. E., and M. E. Raymo (2005), A Pliocene-Pleistocene stack of 57 globally distributed benthic $\delta^{18}O$ records, *Paleoceanography*, *20*, PA1003, doi:10.1029/2004PA001071.
Lunt, D. J., G. L. Foster, A. M. Haywood, and E. J. Stone (2008), Late Pliocene Greenland glaciation controlled by a decline in atmospheric CO_2 levels., *Nature*, *454*, 1102–1105, doi:10.1038/nature07223.
Manley, P. L., and D. W. Caress (1994), Mudwaves on the Gardar Sediment Drift, NE Atlantic, *Paleoceanography*, *9*(6), 973–988.
Maslin, M. A., X. S. Li, M.-F. Loutre, and A. Berger (1998), The contribution of orbital forcing to the progressive intensification of Northern Hemisphere glaciation, *Quat. Sci. Rev.*, *17*, 411–426, doi:10.1016/S0277-3791(97)00047-4.
Mauritzen, C. (1996), Production of dense overflow waters feeding the North Atlantic across the Greenland-Scotland Ridge. Part 1: Evidence for a revised circulation scheme, *Deep Sea Res., Part I*, *43*(6), 769–806.
McCartney, M. S. (1992), Recirculating components to the deep boundary current of the northern North Atlantic, *Prog. Oceanogr.*, *29*, 283–383.
McCave, I. N., and I. R. Hall (2006), Size sorting in marine muds: Processes, pitfalls, and prospects for paleoflow-speed proxies, *Geochem. Geophys. Geosyst.*, *7*, *Q10N05*, doi:10.1029/2006GC001284.
McCave, I. N., and B. E. Tucholke (1986), Deep current-controlled sedimentation in the western North Atlantic, in *The Geology of North America (The Western North Atlantic)*, edited by P. R. Vogt and B. E. Tucholke, pp. 451–468, Geol. Soc. of Am., Boulder, Colo.
McCave, I. N., P. F. Lonsdale, C. D. Hollister, and W. D. Gardner (1980), Sediment transport over the Hatton and Gardar contourite drifts, *J. Sed. Res.*, *50*(4), 1049–1062.
Middleton, G. V. (1966), Experiments on density and turbidity currents: II. Uniform flow of density currents, *Can. J. Earth Sci.*, *3*, 627–637, doi:10.1139/e66-044.
Müller-Michaelis, A., and G. Uenzelmann-Neben (2014), Development of the Western Boundary Undercurrent at Eirik Drift related to changing climate since the early Miocene, *Deep Sea Res. Part I*, *93*, 21–34, doi:10.1016/j.dsr.2014.07.010.
Müller-Michaelis, A., G. Uenzelmann-Neben, and R. Stein (2013), A revised Early Miocene age for the instigation of the Eirik Drift, offshore southern Greenland: Evidence from high-resolution seismic reflection data, *Mar. Geol.*, *340*, 1–15, doi:10.1016/j.margeo.2013.04.012.
Murton, B. J., R. N. Taylor, and M. F. Thirlwall (2002), Plume-ridge interaction: A geochemical perspective from the Reykjanes ridge, *J. Petrol.*, *43*(11), 1987–2012, doi:10.1093/petrology/43.11.1987.
Nielsen, T., P. C. Knutz, and A. Kuijpers (2008), Seismic expression of contourite depositional systems, in *Contourites*, edited by M. Rebesco and A. Camerlenghi, pp. 301–322, Elsevier, Amsterdam.
Olsen, S. M., B. Hansen, D. Quadfasel, and S. Østerhus (2008), Observed and modelled stability of overflow across the Greenland Scotland ridge, *Nature*, *455*, 519–523, doi:10.1038/nature07302.
Parkin, C. J., and R. S. White (2008), Influence of the Iceland mantle plume on oceanic crust generation in the North Atlantic, *Geophys. J. Int.*, *173*, 168–188, doi:10.1111/j.1365-246X.2007.03689.x.
Parnell-Turner, R. E., N. J. White, J. Maclennan, T. J. Henstock, B. J. Murton, and S. M. Jones (2013), Crustal manifestations of a hot transient pulse at 60N beneath the MAR, *Earth Planet. Sci. Lett.*, *363*, 109–120.
Parnell-Turner, R. E., N. J. White, T. Henstock, B. J. Murton, J. Maclennan, and S. M. Jones (2014), A continuous 55-million-year record of transient mantle plume activity beneath Iceland, *Nat. Geosci.*, *7*, 914–919, doi:10.1038/ngeo2281.
Poore, H. R., R. Samworth, N. J. White, S. M. Jones, and I. N. McCave (2006), Neogene overflow of northern component water at the Greenland-Scotland ridge, *Geochem. Geophys. Geosyst.*, *7*, Q06010, doi:10.1029/2005GC001085.
Poore, H. R., N. J. White, and S. M. Jones (2009), A Neogene chronology of Iceland plume activity from V-shaped ridges, *Earth Planet. Sci. Lett.*, *283*, 1–13, doi:10.1016/j.epsl.2009.02.028.
Poore, H. R., N. J. White, and J. Maclennan (2011), Ocean circulation and mantle melting controlled by radial flow of hot pulses in the Iceland plume, *Nat. Geosci.*, *4*,1–4, doi:10.1038/ngeo1161.

Rasmussen, S., H. Lykke-Andersen, A. Kuijpers, and S. R. Troelstra (2003), Post-Miocene sedimentation at the continental rise of Southeast Greenland: The interplay between turbidity and contour currents, *Mar. Geol.*, *196*, 37–52, doi:10.1016/S0025-3227(03)00043-4.
Rebesco, M., and A. Camerlenghi (eds.) (2008), *Contourites*, Elsevier, Amsterdam.
Reid, J. L. (1979), On the contribution of the Mediterranean Sea outflow to the Norwegian-Greenland Sea, *Deep Sea Res.*, *26*, 1199–1223, doi:10.1016/0198-0149(79)90064-5.
Roberts, D. G., and R. B. Kidd (1979), Abyssal sediment wave fields on Feni Ridge, Rockall Trough: Long-range sonar studies, *Mar. Geol.*, *33*, 175–191.
Robinson, M. M., P. J. Valdes, A. M. Haywood, H. J. Dowsett, D. J. Hill, and S. M. Jones (2011), Bathymetric controls on Pliocene North Atlantic and Arctic sea surface temperature and deepwater production, *Palaeogeogr. Palaeoclimatol. Palaeoecol.*, *309*, 92–97, doi:10.1016/j.palaeo.2011.01.004.
Ruddiman, W. F. (1972), Sediment redistribution on the Reykjanes Ridge: Seismic evidence, *Geol. Soc. Am. Bull.*, *83*, 2039–2062, doi:10.1130/0016-7606(1972)83.
Ruddiman, W. F., R. B. Kidd, and E. Thomas (1987), Site 611, *Initial Rep. Deep Sea Drill. Proj.*, *94*, 471–590.
Sandwell, D. T., R. D. Muller, W. H. F. Smith, E. Garcia, and R. Francis (2014), New global marine gravity model from CryoSat-2 and Jason-1 reveals buried tectonic structure, *Science*, *346*, 65–67, doi:10.1126/science.1258213.
Schuler, J., P. A. F. Christie, and R. S. White (2014), Borehole study of compressional and shear attenuation of basalt flows penetrated by the Brugdan and William wells on the Faroes shelf, *Geophys. Prospect.*,*62*, 315–332, doi:10.1111/1365-2478.12087.
Searle, R. C., J. Keeton, R. Owens, R. S. White, R. Mecklenburgh, B. Parsons, and S.-M. Lee (1998), The Reykjanes Ridge: Structure and tectonics of a hot-spot-influenced, slow-spreading ridge, from multibeam bathymetry, gravity and magnetic investigations, *Earth Planet. Sci. Lett.*, *160*, 463–478, doi:10.1016/S0012-821X(98)00104-6.
Shipboard Scientific Party (1996a), Site 984, in *Proceeding of Ocean Drilling Program, Initial Reports* vol. 162, edited by E. Jansen, et al., pp. 169–222, Ocean Drill. Program, College Station, Tex.
Shipboard Scientific Party (1996b), Site 983, in *Proceedings of Ocean Drilling Program, Initial Reports* vol. 162, edited by E. Jansen, et al., pp. 139–167, Ocean Drill. Program, College Station, Tex.
Shipboard Scientific Party, et al. (1972), Site 115, *Initial Rep. Deep Sea Drill. Proj.*, *12*, 361–380.
Smallwood, J. R., and R. S. White (1998), Crustal accretion at the Reykjanes Ridge, *J. Geophys. Res.*, *103*(B3), 5185–5201.
Srivastava, S. P., et al. (1987), *Proceedings of Ocean Drilling Program Initial Reports*, vol. 105, Ocean Drill. Program, College Station, Tex., doi:10.2973/odp.proc.ir.105.1987.
Stolt, R. H. (1978), Migration by Fourier transform, *Geophysics*, *43*, 23–48.
Stow, D. A. V., and J. A. Holbrook (1984), North Atlantic contourites: An overview, *Geol. Soc. Spec. Publ.*, *15*, 245–256.
Vogt, P. R. (1971), Asthenosphere motion recorded by the ocean floor south of Iceland, *Earth Planet. Sci. Lett.*, *13*, 153–160.
Vogt, P. R. (1972), The Faeroe-Iceland-Greenland aseismic ridge and the western Boundary Undercurrent, *Nature*, *239*, 79–81.
Wessel, P., and W. H. F. Smith (1998), New, improved version of generic mapping tools released, *Eos Trans., AGU*, *79*, 579, doi:10.1029/98EO00426.
Wold, C. N. (1994), Cenozoic sediment accumulation on drifts in the northern North Atlantic, *Paleoceanography*, *9*(6), 917–941.
Wright, J. D., and K. G. Miller (1996), Greenland-Scotland ridge control of North Atlantic deep water, *Paleoceanography*, *11*, 157–170.
Wynn, R. B., and D. A. V. Stow (2002), Classification and characterisation of deep-water sediment waves, *Mar. Geol.*, *192*, 7–22.
Zachos, J. C., M. Pagani, L. Sloan, E. Thomas, and K. Billups (2001), Trends, rhythms, and aberrations in global climate 65 Ma to present., *Science*, *292*, 686–693, doi:10.1126/science.1059412.